Cement and Concrete Research 168 (2023) 107156

Contents lists available at ScienceDirect

Cement and Concrete Research

journal homepage: www.elsevier.com/locate/cemconres

Morphology-structural change of C-A-S-H gel in blended cements

Xiaohong Zhu *, Ian G. Richardson

School of Civil Engineering, University of Leeds, Leeds LS2 9JT, United Kingdom

ARTICLE INFO

Keywords:
SCMs
Morphology
C-A-S-H gel
Nano-structural change

ABSTRACT

Pastes of white Portland cement (wPC) and wPC-30 % pulverized fuel ash (PFA), -60 % ground granulated blast furnace slag (GGBS), -30 % or 60 % inert filler (anatase-type TiO_2) blends were prepared to investigate the dominant factors for morphological change of outer product (OP) C-A-S-H gel in blended cement systems. The OP C-A-S-H gel in SCMs-blended cements changes its morphology from fibrillar-like to mixed fine-fibrillar/foil-like when its Ca/(Si + Al) ratio < 1.30 and Al/Si ratio > 0.15. Meanwhile, the fine-fibrillar/foil-like C-A-S-H has the mean length of the aluminosilicate chain longer than 7– 8, of which, the [SiO_4] bridging site occupancy factor (SOF_{BT}) is higher than 0.6 and the [AlO_4] SOF_{BT} is higher than 0.3. The pore solutions show the characteristics of effective saturation index (ESI) of CH < −0.15 and ESI of jennite-based C-S-H gel < 0.10. The morphology of C-A-S-H gel in inert filler blends remains fibrillar throughout the hydration.

1. Introduction

Supplementary cementitious materials (SCMs) are used extensively in modern concrete to help reduce the carbon emission from cement industry and to enhance the durability of the concrete [1]. SCMs are sources of additional Al (except for silica fume) and Si during hydration, which results in compositional changes of C-(A-)S-H gel [2]. The addition of SCMs such as pulverized fuel ash (PFA) [3] or ground granulated blast furnace slag (GGBS) [4] reduces the Ca/Si ratio and increases the Al/Si ratio of C-A-S-H gel, and its morphology changes at the later age of hydration [3,4]. The C-(A-)S-H gel – quantitatively the most important binding phase in cementitious materials – thus shows variable composition, morphology, and properties in blended cements [5–7]. The morphology of outer product (OP) C-(A-)S-H gel defines the capillary pore structure of pastes, which affects the long-term mechanical and transport properties that determine the durability [7]. Therefore, understanding the morphological changes of C-A-S-H gel due to the addition of SCMs is crucial for the assessment of the durability of the materials. The OP C-(A-)S-H gel in either C_3S or Portland cement shows a typical fibrillar-like morphology [2,8,9], but will change to foil-like when PFA [3] or GGBS [4] react to a certain degree. The morphological changes of C-(A-)S-H gel coincide with changes in its composition, nano-structure, and the solution environment [3,8,10]. The purpose of this paper is to demonstrate the morphological changes of C-A-S-H gel in blended cements after the reaction of SCMs and to identify the dominant factors that affect this change. Two SCMs, PFA and GGBS, were used to partially replace the white Portland cement (wPC); one inert filler, anatase-type TiO_2, was used for comparison, replacing the same percentage of wPC. The pastes were examined using analytical transmission electron microscopy (TEM), ^{29}Si magic angle spinning (MAS) nuclear magnetic resonance spectroscopy (NMR), X-ray diffraction (XRD) and thermal analysis.

2. Experimental

A commercial white Portland cement (Hanson Castle, UK), anatase-type TiO_2 (Sigma-Aldrich, UK), PFA (Drax, UK) and GGBS (Francis Flower, UK) were used in this study. Bulk oxide compositions are given in Table 1. Iron-rich particles were hand-removed from PFA using a magnet to reduce their impact on the NMR experiments (the detailed procedure is given in Ref. [3]). Other information on the raw materials is given in the Supplementary materials.

Five cement pastes were studied: neat wPC, 30 % PFA or TiO_2-70 % wPC, and 60 % GGBS or TiO_2-40 % wPC. A water/binder (w/b) ratio of 0.50 was used for all pastes. The blended powders were pre-stirred for 5 min. All five cement pastes were hand-mixed for 2 min and cast into 8 mL plastic tubes. These tubes were sealed with Parafilm and rotated continuously for 24 h at 9 r/min to avoid bleeding. The specimens were then cured in a water bath at 25 °C for 1, 3, 7, 14, 28, 91, and 270 days (except for those used at 5 h). The samples were crushed and hydration-stopped using solvent exchange with isopropanol (IPA), followed by drying in a vacuum desiccator. The treated samples were ground into

* Corresponding author at: Department of Civil and Environmental Engineering, the Hong Kong Polytechnic University, Kowloon, Hong Kong.
E-mail address: xiaohong.zhu@polyu.edu.hk (X. Zhu).

https://doi.org/10.1016/j.cemconres.2023.107156
Received 18 May 2022; Received in revised form 19 January 2023; Accepted 13 March 2023
Available online 28 March 2023

fine powder prior to analysis.

Isothermal conduction calorimetry (ICC) experiments were conducted at 20 °C using a TAM-Air (TA Instruments, USA) with 8 twin-channels with quartz as the reference. Prior to the experiments, all of the raw materials including DI water were placed in a room with constant temperature of 20 °C for around 3 h. 9 g of paste (6 g of binder and 3 g of DI water) was placed into a 20 mL ampoule. An external mixing method [3] (2 min shaken on an orbital shaker) was used and the ampoules were immediately moved to the equipment. Around 20 min was used for equilibration, which was needed due to opening of the sample chamber. The measurements were carried out for 3 days. Two replacement levels for GGBS, PFA and anatase were selected for comparison.

The CH content of the wPC, GGBS/wPC, PFA/wPC pastes was determined by QXRD using the G-factor method with corundum (α-Al_2O_3) as the external standard [11]. The internal standard method was used for anatase (TiO_2)-containing samples for all ages [12]. Hydration stopped samples were ground into fine powder and back-loaded into the sample holder. All data except those for 270 days blended wPC samples were collected using a Bruker D2 Phaser (CuKα radiation; 30 kV; 10 mA) with a step size of 0.01°, dwell time of 1.0 s, rotation of 15 rot/min, and range of 5–70° 2θ. The 270 day samples were collected using a Philips X'Pert system with the same settings other than a range of 5–80° 2θ. Patterns for corundum were collected using the same conditions to determine the G-factor. The chemically bound water that was used for the calculation of the mass attenuation coefficient (MAC) was calculated from the TGA data.

The hydrated wPC samples (15–18 mg each) were analysed using a Stanton Redcroft Simultaneous Thermal Analyser STA 780 (UK) under N_2 atmosphere with a heating rate of 20 °C/min. An empty platinum crucible was used as the reference and the testing temperature range was from room temperature (about 20 °C) to 1000 °C. The raw materials (20–40 mg) were analysed under the same conditions using a Netzsch Simultaneous Thermal Analyser 449 F5 Jupiter (Germany) equipped with a mass spectrometer. The portlandite (CH) content was calculated using the tangent method with the consideration of mass loss from raw materials. The details of the calculation methods for CH are provided in the Supplementary materials.

^{29}Si MAS NMR spectra were collected by a Bruker Avance III HD (WB magnetic field 9.4 T; operating frequency of 79.48 MHz for ^{29}Si). All the experiments were run at the magic angle of 54.74°, which was set by observation of ^{79}Br resonance from KBr. Samples for NMR were freshly ground and packed into 7 mm zirconia rotors with KEL-F caps and spun at 6 kHz. Since the natural abundance of ^{29}Si is only 4.67 %, longer scans are normally required for cement pastes to achieve quantitative spectra. In this work, the ^{29}Si MAS NMR spectra were acquired over 4096 scans (all PFA-containing samples except 91 days) or 2048 scans (all other samples) using a pulse recycle time of 40 s, a pulse duration (width) of 5.5 μs (90° flip angle) for an RF field strength of 45 kHz, and an acquisition time of 40 ms. TMS (tetramethylsilane) was used as the reference. Deconvolutions of ^{29}Si MAS NMR spectra were performed using a user-made procedure for Igor Pro (WaveMetrics, USA) initially developed by Brough [13]. The Voigt line shape (mixture of Cauchy-Lorentz and Gaussian line shapes) was used for all peaks. Calculations with the NMR results were carried out using the equations provided in Refs. [2,14].

Samples used for transmission electron microscopy (TEM) were prepared as follows. Slices (around 1–2 mm thick) were cut from the hardened cement paste cylinders using a Buehler (USA) IsoMet™ low-speed saw with a diamond blade. The slices were hydration stopped using isopropanol and dried in a desiccator. The dried slice was then attached to a clean glass slide with cyanoacrylate glue and thinned by hand using progressively finer SiC papers (#500, #800, #1200, and #2000, corresponding to the grain size of 30, 22, 15, and 10 μm) until a thickness of approximately 30 μm. The thinned slice was removed by immersion into acetone and glued between two 3 mm diameter copper TEM grids using epoxy. The grid had a hole with dimensions of 2 × 1 mm, which allowed the sample to be argon ion-beam milled in a Gatan Precision Ion Polishing System (PIPS). The aim of ion milling is to form a hole in the centre of the specimen, with the region around the hole being sufficiently thin to be electron transparent. The Gatan PIPS was vacuum-worked at 3–4 keV with a milling angle in the range of 4–6°. The lower milling angle (glancing incidence) vastly reduced the input energy, preventing damage due to thermal affects. The whole PIPS process for each sample lasts for around 40–50 h. Samples were then stored under vacuum and carbon-coated using an Agar Scientific Turbo Carbon Coater to prevent charging during TEM examination. The TEM experiments were carried out using a FEI Titan3 Themis 300 microscope operating at 300 kV with a FEI Super-X 4-detector energy-dispersive X-ray analysis (EDX) system. Images were taken at magnifications ranging between ×5k to ×20k. EDX analyses were performed at ≈ ×20k with a spot size of 3 and live time of 10 s. The OP C-A-S-H gel in blended wPC systems (between 10 and 12 regions) were the main areas of interest. Before each EDX analysis, the selected area electron diffraction (SAED) was used to check that the analysis region was C-A-S-H gel that was free of intermixture with crystalline phases. In addition, thinner parts were chosen for EDX analysis to avoid the absorption of emitted X-rays and allow straightforward quantification.

The pore solution of cylindrical paste samples (⌀2.5 cm × 6.0 cm) was extracted under a constant pressure of 407.6 MPa (800 kN over 1962.5 mm^2) for 45 min. A vacuum pump was used to avoid carbonation of the collected solution. Extraction of pore solution from mature paste samples is very difficult and it was necessary to use 2 or more cylinders of each sample in order to obtain enough solution for analysis. The element concentrations in the collected solutions were tested by an ICP-OES (Perkin Elmer optima 8000, USA) using argon plasma. The equipment was pre-heated for around 30 min to achieve a stable plasma condition. The filtrated samples (0.45 μm PTFE Springe Filter) were acidified with proper levels of 5 mol/L HNO_3 and diluted with deionized water to end up with a pH value of around 1.0. Samples were filtered/diluted prior to ICP-OES analysis because the equipment is very sensitive to total solids and the alkali ions in the solution. Some important issues are summarised by Vollpracht et al. [15] and Dean [16]. The thermodynamic modelling for the calculation of the saturation levels was performed with PHREEQC V3.4.0 using the database provided by Lothenbach [17].

3. Results and discussion

3.1. Hydration process of blended wPC

Fig. 1 shows the effect of 30 % filler or SCMs on the hydration process of wPC. In Fig. 1b and c, the black dash line represents the hydration heat of neat wPC multiplied by 0.7. In the heat flow curves, it is very clear that three hydration peaks occur between 5 and 24 h. The

Table 1
Bulk oxide compositions of GGBS, PFA, and wPC (by mass %) determined by XRF.

Composition	SiO_2	Al_2O_3	Fe_2O_3	MgO	CaO	Na_2O	K_2O	SO_3	$LOI_{900°C}$
GGBS	35.07	12.43	0.41	8.41	40.67	0.38	0.58	0.78	−0.15
Fe-removed PFA	51.26	25.27	6.80	1.78	2.47	1.98	3.57	0.48	4.03
Residual PFA	49.02	24.38	10.92	1.59	2.43	1.42	3.46	0.47	4.07
wPC	24.49	2.09	0.30	0.59	68.08	0.25	0.09	1.95	0.95

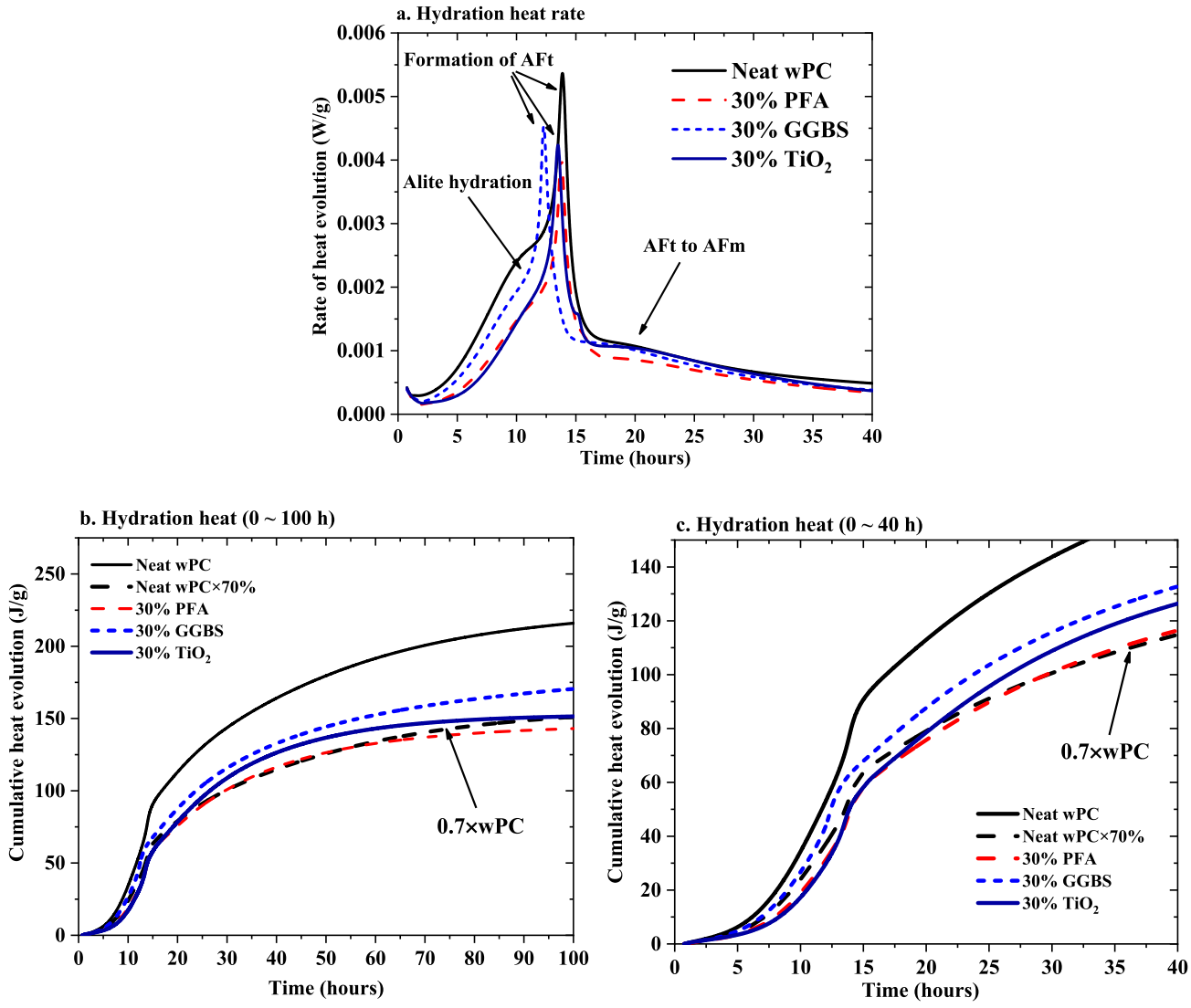

Fig. 1. (a) Rate of heat evolution, (b) cumulative heat evolved (up to 100 h) and (c) cumulative heat evolved (0– 40 h) of neat wPC, 30%PFA-wPC, 30 % slag-wPC, and 30%TiO_2-wPC pastes.

dominant peak is due to alite hydration, with a first shoulder peak representing AFt formation and a second shoulder peak indicating AFm formation [18]. For all the samples with SCMs or filler replacement, both the first and second hydration peaks are reduced. This is due to the initial lower hydraulic properties of these fillers. The AFt formation peak is accelerated by the addition of GGBS, but not by the PFA or TiO_2. The GGBS gives a higher and faster heat evolution curve when compared to that of PFA and anatase added samples, which is attributed to the self-hydraulic nature of GGBS [18–20]. The curves in Fig. 1c show that the heat evolution within 20 h for the 30 % PFA and TiO_2 samples is the same and that it is lower than value for the 0.7 wPC curve, i.e. the heat that would be expected upon simple dilution. This result is not consistent with Berodier et al.'s [21] view of the 'filler effect' during the early age hydration of cement; however, it is the same as Richardson et al.'s results [3]. This shows that the PFA or TiO_2 have an initial retarder effect on wPC hydration. The 'filler effect' cannot be simply explained as the increase of extra surfaces for nucleation, which should be the effects of either a higher nucleation density or a higher growth rate of C-(A-)S-H gels [21]. The microscopical observations by Berodier et al. [21] indicated that the filler showed little or no effect on the growth rate of individual C-S-H needles. Instead, the shearing between particles was found to be one of the dominant factors that can generate more nuclei in blended cements. In the current study, the cement slurry was mixed for 2 min on a batch orbital shaker (~300 rpm), which was much slower than Berodier et al.'s work (1600 rpm–15,000 rpm). The differences in shearing rate may result in different heat evolution behaviours of blended cements. In contrast, GGBS has a totally different hydration curve compared to that of PFA or TiO_2, which gives a much higher cumulative heat than the reference curve (i.e. wPC × 0.7). The main reason is also due to the self-hydraulic property of GGBS [19]. The curves passed the reference curve (i.e. wPC × 0.7) at around 20 h for the TiO_2 sample and at around 30 h for the PFA sample, which indicate the start of the 'filler effect' (i.e. a point where the hydration of wPC in the blends is accelerated). These results are similar to those summarised by Richardson et al. [3] in which the cumulative heat curves of two PFA-containing samples surpassed the reference at around 25 h. The same effects are found in 60 % fillers or SCMs added samples, which are given in the Supplementary materials.

3.2. *Phases present in blended wPC and $Ca(OH)_2$ content evaluation*

The crystalline phases in all blended wPC pastes were identified by XRD (see the Supplementary materials), and included unreacted alite and belite, CH, and AFt; additional hydrotalcite-like phase was found in

GGBS blends after 3 d of hydration; unreacted mullite (in PFA), melilite (in GGBS), and anatase remained in the blends throughout the hydration.

Fig. 2a and b shows how the CH content (percentage of ignited mass) developed with age for the both 30 % and 60 % replacement level systems determined by TG-DSC analysis. The CH content increased over hydration time. The unfilled circles in these two graphs represent the CH of neat wPC multiplied by 0.7 or 0.4 for the purpose of comparison, which can be therefore regarded as the reference data (denoted as CH^{exp}) for the SCMs/filler added samples based on simple dilution [3,4]. The measured CH contents in the blended system are denoted as CH^{act}. The ratios of CH^{act} to CH^{exp} were calculated for each blend and are plotted in Fig. 2c.

Fig. 2c shows that the samples containing PFA and TiO_2 have a lower CH content than expected at 5 h, indicating that initial hydration of wPC in the blends is retarded. In contrast, the value of CH^{act}/CH^{exp} for 60 % GGBS is >1, indicating acceleration. These results are consistent with the conduction calorimetry results shown in Fig. 1. The initial retarder effect of PFA was also observed by Richardson et al. [3], who noted that there have been considerable differences in the effects of PFA on cement hydration reported in the literature: some studies report retardation of the hydration of the aluminate phase, some support retardation of the hydration of the silicate phases, and some consider that both aluminate and silicate hydration are retarded; on the other hand, some studies report a totally opposite view. It is evident that the mechanism regarding the effects of PFA particles on the hydration of cement is complex and is affected by the characteristics of the materials and the hydration environment. The results in the current study support the view that the aluminate reaction is not significantly affected by 30 % PFA but slightly retarded by 60 % PFA (see the Supplementary materials); whereas the silicate reactions are initially retarded significantly by replacing 30 %–60 % PFA (see Fig. 1 and Fig. S6 in the Supplementary materials). These results are also supported by the CH data, which gives a CH^{act}/CH^{exp} ratio lower than 1 at early age, indicating initial retardation of the silicate reactions.

However, the values of CH^{act}/CH^{exp} for TiO_2/PFA-containing samples shown in Fig. 2c rise at intermediate ages, which indicates an acceleration of the silicate reaction during this period (the so-called 'filler effect'). After around 3 day hydration, the CH^{act}/CH^{exp} ratio of PFA blends drop down, which indicates the commencement of the pozzolanic reaction of the glassy phase in the PFA; whereas the CH^{act}/CH^{exp} ratios of TiO_2 blends remain higher until 270 days, which means that TiO_2 does not consume CH and a higher hydration degree is achieved. This result is also supported by the lower residual clinker peaks in TiO_2 blends in XRD patterns (see the Supplementary materials). As expected, the PFA and GGBS consume CH and CH^{act}/CH^{exp} ratios in these two systems gradually decrease with age to values that are lower than 1. The 'changing ages' (from >1 to <1) from TG for 30 % PFA and 60 % GGBS blends are around 40 days and 14 days, respectively. The same information but obtained from QXRD analysis regarding CH^{act}/CH^{exp} ratios is given in Fig. S12 in the Supplementary materials.

Fig. 3 shows a plot of the bound water in hydrates against age calculated from TG-DSC analysis data. The unfilled circles represent the expected chemically combined water (CW^{exp}) multiplied by the wPC content (i.e. ×0.7 and ×0.4) based on the simple dilution. The measured bound water in blends is denoted as actual bound water (CW^{act}). The ratio of CW^{act}/CW^{exp} was calculated and given in Fig. 3c. The chemically bound water is present in both C-A-S-H gels and crystalline phases. It is notable that the CW^{act}/CW^{exp} ratio of GGBS blends is always higher than 1, which supports the acceleration of hydration of cement. This value is much higher than those for TiO_2 and PFA blends. This is due to the self-hydraulic property and higher reactivity of GGBS that can generate more hydrate phases (including crystalline LDH phases; see XRD results in the Supplementary materials) and therefore more bound water [22,23]. An extreme high CW value for the 60 % TiO_2 blend is found at 5 h, which is perhaps due to flocs of the nano-scale particles (see the PSD in the Supplementary materials) trapping water that is difficult to remove during the hydration-stopping process.

Comparison between CW^{act}/CW^{exp} and CH^{act}/CH^{exp} is given in Fig. 4 for the purpose of identifying the reason for the increasing CW^{act}/CW^{exp} ratio. The relationship between these two ratios is shown in Fig. 4a for the TiO_2 (inert filler) blends and in Fig. 4b for the SCMs (GGBS and PFA). As confirmed by XRD (Supplementary materials), the hydration products are the same in the TiO_2 blends as in the neat cement, and so any additional bound water must be due to greater quantities of those phases and thus to acceleration of the silicate reactions.

A good correlation between CW^{act}/CW^{exp} and CH^{act}/CH^{exp} is observed for the TiO_2 blends, as shown in Fig. 4a, which means that the TiO_2 accelerates the hydration of the cement at later ages and generates more hydration products (i.e. CH and C-S-H gel). In comparison to the TiO_2 blends, the SCM blends give different relationships between CW^{act}/CW^{exp} and CH^{act}/CH^{exp}. GGBS generates more CH and more bound

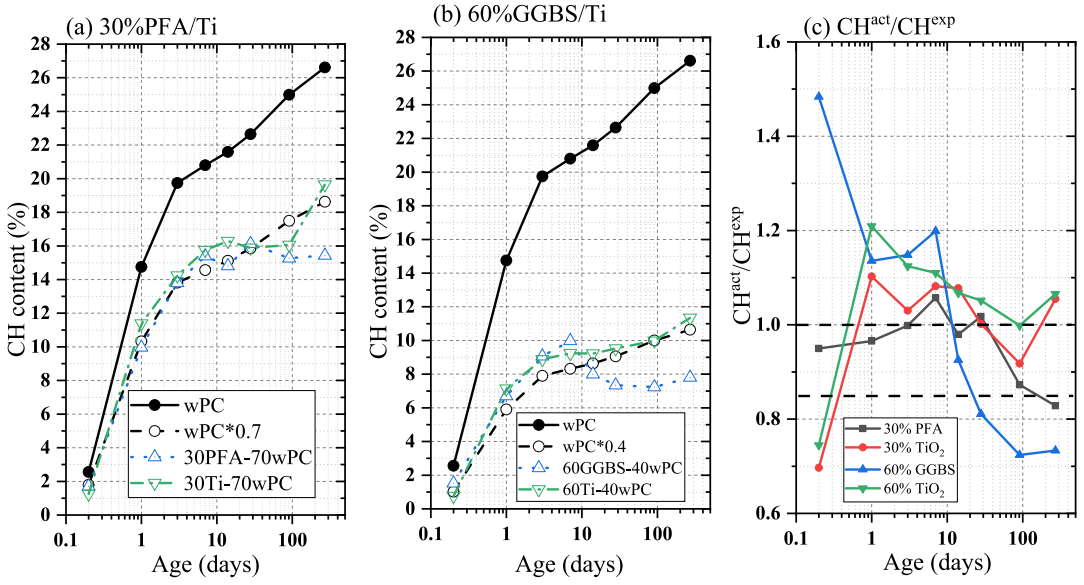

Fig. 2. CH content evaluation from TG-DSC: (a) at 30 % replacement level; (b) at 60 % replacement level; (c) calculated parameter CH^{act}/CH^{exp}. where CH^{act} is the actual CH content in blended cement and CH^{exp} is the expected CH content calculated by the percentage of wPC.

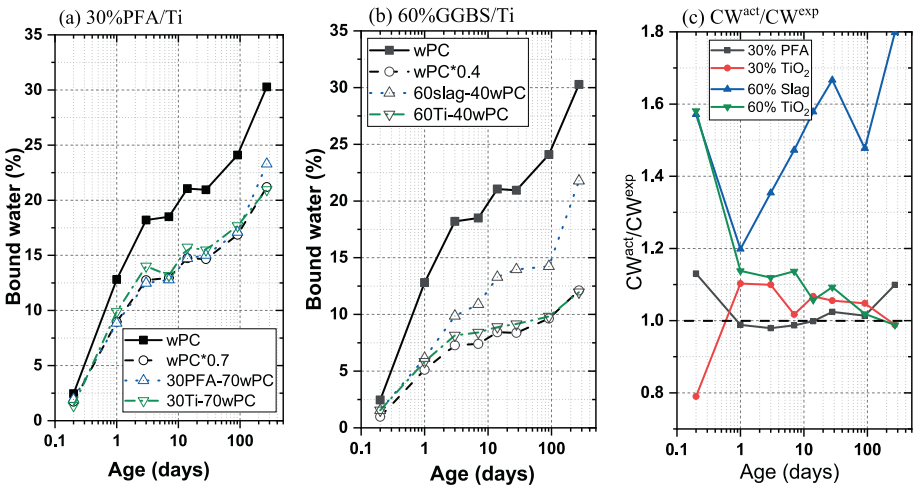

Fig. 3. Chemically bounded water determined by TG-DSC: (a) at 30 % replacement level; (b) at 60 % replacement level; (c) calculated parameter CW^{act}/CW^{exp}.

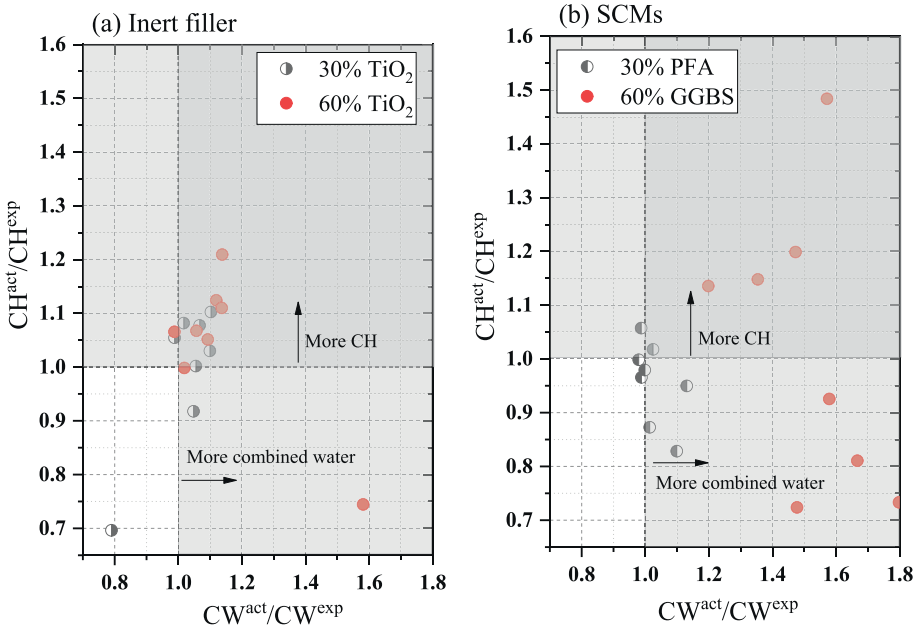

Fig. 4. Relationships between CW^{act}/CW^{exp} and CH^{act}/CH^{exp} (calculated from TG-DSC analysis) in a. inert filler (TiO_2) and b. SCMs-blended wPC systems.

water than 'expected', and the quantity of bound water is greater than that derived solely from the extra CH. This observation is supported by the conduction calorimetry results, Section 3.1. The extra CH results from the accelerated hydration of the Portland cement and the extra bound water is from the extra CH, C-A-S-H gel and also LDH phases (AFm and Mg,Al LDH phases are identified on the XRD patterns; Supplementary materials). The deviation from the slope that is observed for the TiO_2 blends (when compared with GGBS blends) is due to the participation of the glassy GGBS in the hydration reactions. For the PFA blends, the values of CW^{act}/CW^{exp} and CH^{act}/CH^{exp} are both around 1 at intermediate ages, the latter having risen from below 1, consistent with a slight acceleration effect of the PFA particles. Commencement of the reaction of the glassy phase in both SCM-blends is associated with the consumption of CH and formation of C-A-S-H gel, which results in values of CH^{act}/CH^{exp} and CW^{act}/CW^{exp} that are respectively lower and higher than 1.

3.3. ^{29}Si NMR analysis of blended wPC samples

3.3.1. Experimental observations

Fig. 5 shows the ^{29}Si MAS NMR spectra and the deconvolution of all blends hydrated for 270 days. Spectra for other ages (7, 14, 28, 91 days) are given in the Supplementary materials. The results from deconvolution are shown in Figs. 6 to 10. The same peaks related to the possible structural silicate units but with different intensities are assigned to these blended cements, which include monomer (belite, Q^0) at ≈−71.3, chain-end tetrahedra (Q^1) at ≈−79.2, and middle-chain tetrahedra at ≈−81.5 for $Q^2(1Al)$ or ≈−85.2 ppm for $Q^2(0Al)$ [2,20,24]. In addition, a small peak due to monomers in γ-C_2S is present throughout all blends and samples. For GGBS and PFA blends, additional peaks that belong to glassy PFA at ≈−106.8 (Q^4) and GGBS at ≈−76.0 ppm are assigned to remove the effect of unreacted SCMs [3,4,25,26]. A small Q^{0H} peak throughout the hydration has often been assigned at a chemical shift quite close to γ-C_2S [3,13] but this peak is ignored in this work due to its small size and the overlap with the γ-C_2S.

Fig. 6 shows the distribution of silicate anion units in the C-A-S-H

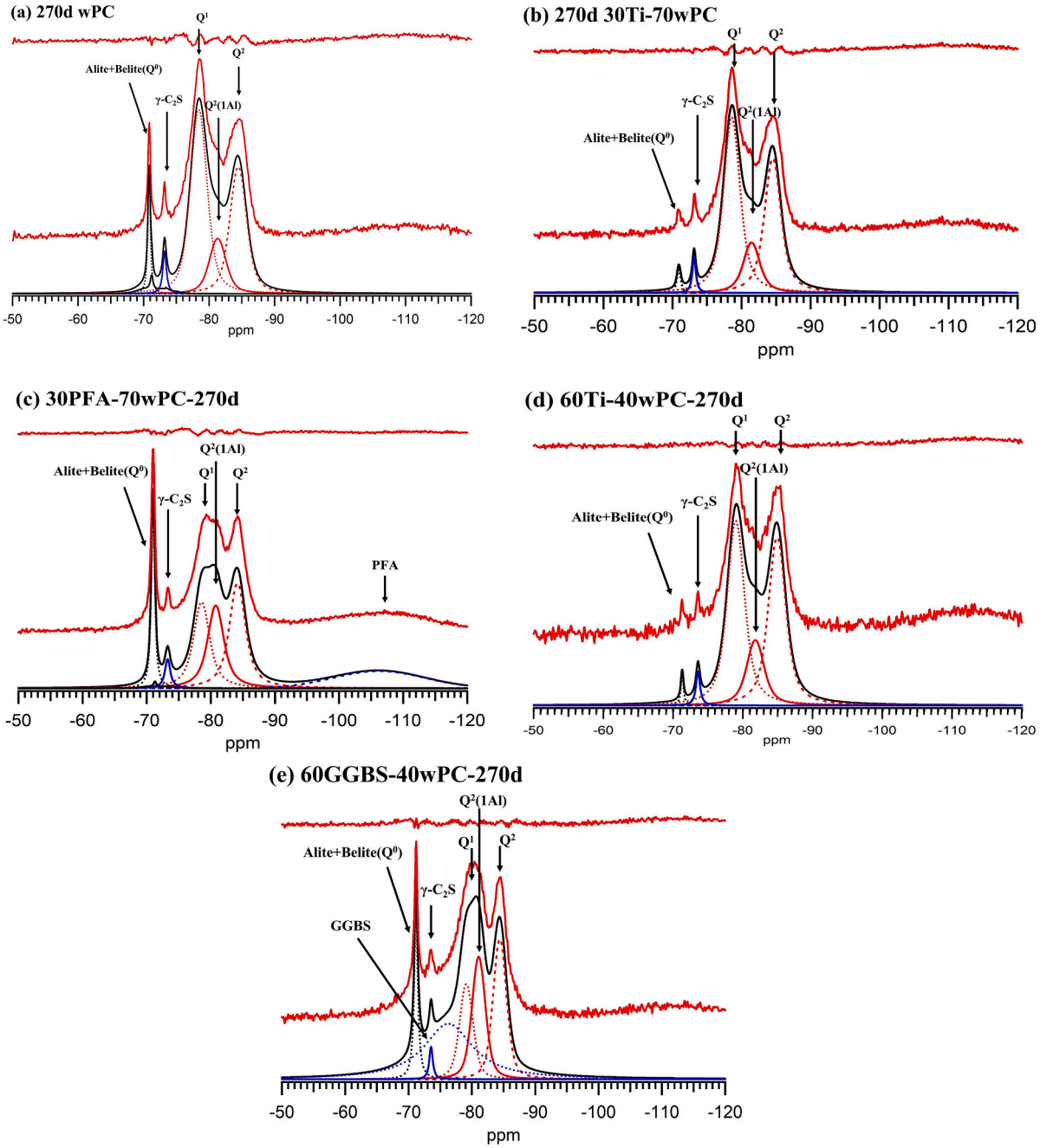

Fig. 5. Examples of ^{29}Si MAS NMR results of blended cements: (a) 270d wPC; (b) 270d 30Ti-70wPC; (c) 270d 30PFA-70wPC; (d) 270d 60Ti-40wPC; (e) 270d 60GGBS-40wPC. The deconvolution of other-age samples can be found in the Supplementary materials.

phase in different blends from 7 to 270 days. The data are normalized to 100 % to indicate more clearly how the relative amounts of the silicate species change with age.

It is clear that the early-age (7 days) C-A-S-H is dominated by Q^1 in neat wPC and TiO_2 blends (≈65–70 %), which is consistent with previous studies that concluded that the dominant silicate group is dimer at early hydration of either C_3S paste [13] or neat wPC [3]. In the PFA blend at the same age (Fig. 6c), the fraction of Q^1 is slightly lower at around 60 % but the Q^2(1Al) is similar, which are consistent with acceleration of the alite reaction and no reaction of the PFA. In GGBS blend at 7 days, the fraction of Q^1 is lower at 50 % accompanied by a larger fraction of Q^2(1Al) (i.e. from ≈12 % in neat wPC to ≈ 20 %), which are consistent with some reaction of the glassy GGBS.

The fraction of Q^1 tetrahedra decreases with age in the neat wPC paste and the TiO_2 blends until 91 days and then remains stable until 270 days, accompanied by an increase in Q^2(0Al) but stable Q^2(1Al). This observation is caused by the limited alumina sources that are present in the wPC system. Overall, the TiO_2 blends possess higher fractions of Q^2 compared with that of the neat wPC paste, which is consistent with the lower intensity of Q^0 that means a higher hydration degree of silicate phases is achieved throughout the testing ages. In contrast, PFA blends show a continuous decreasing trend of Q^1 tetrahedra and an increasing trend of Q^2(1Al) units, which shows evidence for the PFA reaction. However, the fraction of Q^2(0Al) remains quite similar to that in neat wPC and TiO_2 blends. The silicate tetrahedra distribution, especially Q^2(1Al) units, is different in GGBS blends. Specifically, the fraction of Q^1 tetrahedra drops dramatically between 7 and 14 days, accompanied by increased Q^2(1Al) but limited change to Q^2(0Al). This result indicates

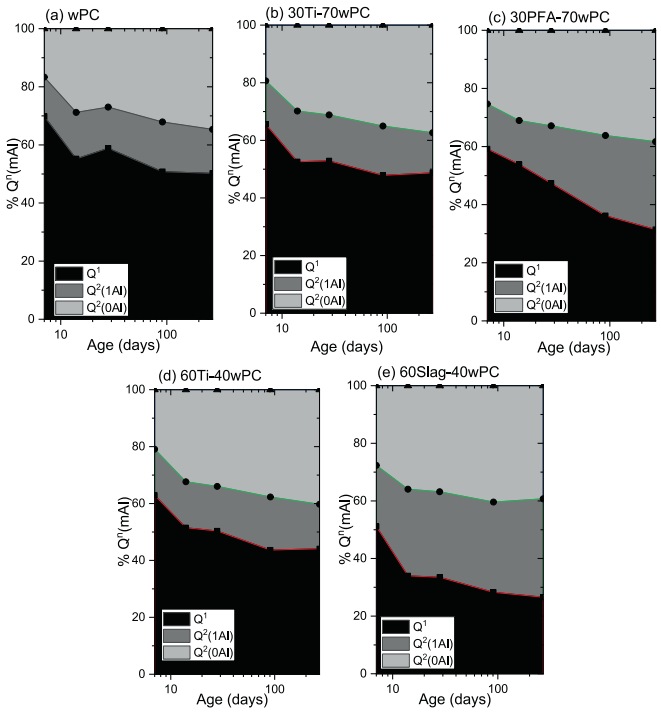

Fig. 6. Normalized silicate species distribution of blended cements against time: (a) 270d wPC; (b) 270d 30Ti-70wPC; (c) 270d 30PFA-70wPC; (d) 270d 60Ti-40wPC; (e) 270d 60GGBS-40wPC.

that the reaction of GGBS is fast during the corresponding ages (7–14 days) but slows down thereafter. In comparison with neat wPC or TiO_2 blends, the fraction of Q^2(1Al) tetrahedra is significantly larger after 30 and 14 days in PFA and GGBS blends respectively.

An interesting observation is that the fraction of Q^2(0Al) is quite similar at 270 days in all of the samples (≈35–40 %, i.e. over 1 in 3), which agrees with Richardson et al.'s study of water- and KOH-activated PFA blends [3]. The main variation is the relative amounts of Q^1 and Q^2(1Al) (i.e. the end-chain tetrahedra and the paired tetrahedra that are adjacent to the Al—O 'bridging' tetrahedra (BT)). These data support the view that the main difference in C-A-S-H between SCM blends and inert filler/neat cement blends is the incorporation of additional Al at bridging sites only, which further lengthens the silicate chains of C-A-S-H [3,27,28]. Thus, the increase in the fraction of Q^2(1Al) tetrahedra is an indicator for the reaction of SCMs, but not a sign of the start of the reaction. As shown in Fig. 6, it can be confirmed that PFA reacts continuously and slowly between 30 days (i.e. the Q^2(1Al) fraction is greater than the highest value in $30TiO_2$ blends) to 270 days and GGBS reacts between (but not starting at) 10 days (i.e. the Q^2(1Al) fraction is greater than the highest value in $60TiO_2$ blends) to 270 days.

Fig. 7 shows the hydration degree of the silicate phases in the clinker (i.e. alite + belite) against age for different blends, as determined by NMR. As expected, the inert filler (TiO_2) blends give higher hydration degree all through 7 to 270 days, which is consistent with the results of CH^{act}/CH^{exp} as shown in Fig. 2. This experimental phenomenon is believed to be brought about by the 'filler effect'. Similarly, a higher hydration degree of (alite + belite) is achieved in the PFA blend at 7 days, which can also be attributed to the 'filler effect'. However, lower hydration degrees of PFA blends are found afterwards. The same results are found in GGBS blends throughout 7 to 270 days. The decreased hydration degree of silicate phases in PFA and GGBS blends is plausibly related to the hydration of the glassy phases, which provide Si and Al for the formation of C-A-S-H, thus decreasing the requirements of silicate phases in the clinker. In summary, from the CH data, the crossover for PFA happened at around 60 h (i.e. the 'filler effect' kicked in at around 60 h), whilst from the NMR data, it appears that a second crossover occurs at around 14 days, when the reaction of the clinker is again retarded.

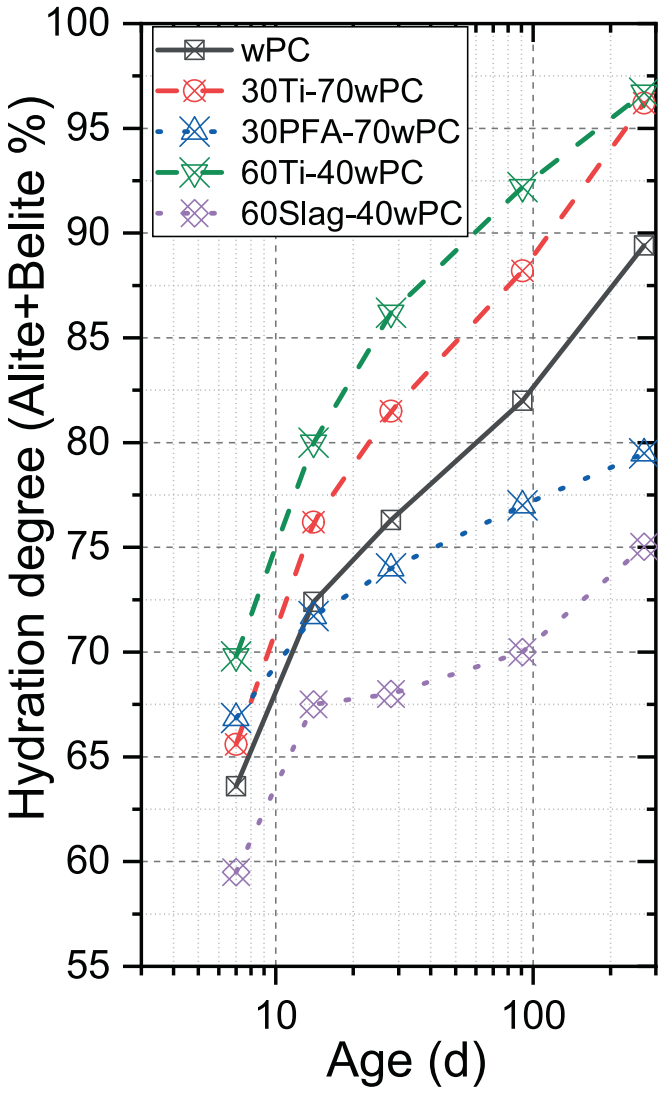

Fig. 7. Hydration degree of silicate phases (alite + belite) of blended cements calculated through quantitative NMR.

3.3.2. *Nanostructure development of C-A-S-H gel in blended wPC*

The increased polymerization of silicate tetrahedra results in up-field chemical shifts in NMR spectra [29]. Many studies have confirmed a 6 ppm up-field difference in the chemical shift of Q^2 tetrahedra when compared to Q^1 (at ≈−79 ppm) in ^{29}Si NMR spectra e.g. [29–32]. The chemical environments of Si—O tetrahedra are further affected by the replacement of Si by Al at bridging sites in an aluminosilicate chain [27], which generates a down-field chemical shift of ≈3–5 ppm [3,27,33]. Therefore, the peak at ≈−82 ppm in ^{29}Si MAS NMR spectra has been assigned as Q^2(1Al) in many studies [2,20,24,27,34,35], and the assignment is supported strongly by the excellent agreement between the Al/Si ratio of the C-A-S-H calculated from the results of the deconvolution of the NMR spectra with the value measured directly by analytical TEM (as shown in Fig. 17 in [35] and Fig. 11 in [3]). More than three peaks have been used by some other workers. As an example, Yang et al. [36] assigned a peak at −86.7 ppm to a second type of Q^2P (pair) site, but that peak was only observed with C-A-S-H that had a very low Ca/Si ratio (0.6 to 0.8) and extremely long Al—Si chains, and they assigned peaks at around −81 ppm and around −82 ppm to Q^2P(1Al [4]) and Q^2B (bridging) sites respectively. However, since it is not possible to

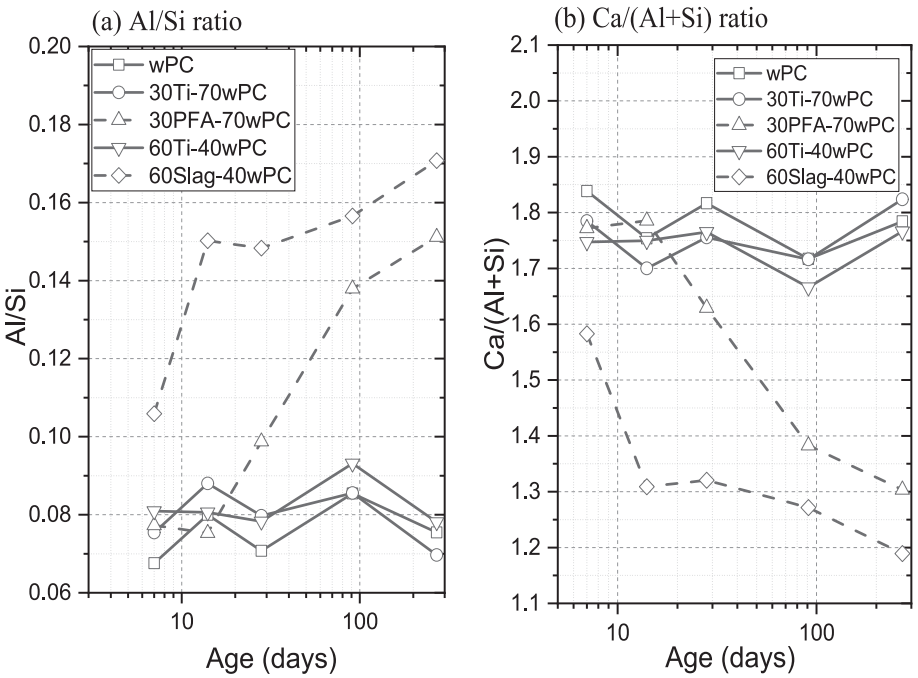

Fig. 8. (a) Al/Si ratio (determined by NMR results) and (b) Ca/(Al + Si) ratio (calculated using the universal relationship in [3]) development against time.

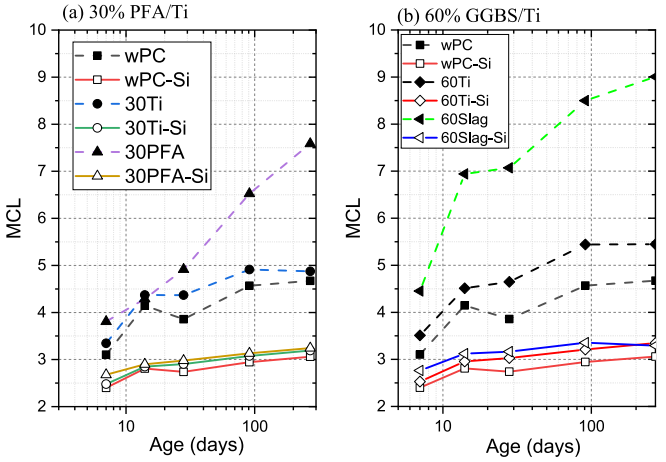

Fig. 9. MCL and MCL_{si} of blended samples at (a) 30 % replacement level and (b) 60 % replacement level.

resolve these different peaks in the one-dimensional ^{29}Si spectra collected in the present study, and given the general agreement between Al/Si ratios determined by TEM-EDX and those calculated from ^{29}Si NMR when using three peaks for C-A-S-H during the fitting procedure, no attempt was made to use more than three peaks.

The Al/Si ratio calculated from the results of the quantitative NMR of all blends is shown in Fig. 8a. Unsurprisingly the Al/Si ratios of the C-A-S-H in the neat wPC and TiO_2 blends are essentially the same and they remain stable in a range of ≈ 0.07–0.09, which corresponds to the stable value for $Q^2(1Al)$ in Fig. 6. The PFA and GGBS blends show a completely different development trend of Al/Si ratio for the C-A-S-H. For the GGBS blend, the Al/Si ratio reached >0.10 at 7 days and rose to ≈0.17, which indicates that the glassy GGBS started to react before 7 days and continuously hydrated until 270 days. The PFA blend initially possesses a comparable Al/Si ratio with neat wPC or TiO_2 blends, followed by a steep increase to ≈ 0.15 at 270 days, which illustrates that PFA reacted mainly after 2 weeks. These results agree with the CH content evaluation from TG-DSC analysis in Fig. 2.

Fig. 9 shows how the mean silicate chain length (MCL) and MCL_{Si} (i.e. the value for just the silicate portions) of the aluminosilicate chains in the C-A-S-H vary with age for all the cements in this study (calculated from the NMR results). A similar study on 30 % PFA blended cements [3] showed that the MCL increased from an initial value of ≈3 before 28 days up to ≈10 after 1 year and 14 after 13 years, whereas the C-A-S-H in the neat wPC also had a MCL of ≈3 before 28 days, but increased to only 4.4 after 1 year and ≈5 after 4 years. The results plotted on Fig. 9 are consistent with the earlier work. Inspection of the figure shows that: (i) neat wPC has an MCL ≈ 3 at 7 days and increases to ≈4.5 at 270 days; (ii) the MCL for the TiO_2 blends are slightly higher than for the neat wPC, which is attributed to the higher hydration degree; (iii) the values for the 30 % PFA blend are comparable with the neat wPC before 28 days (≈3–5) but then increase to ≈7.5 at 270 days; (iv) the MCL for the 60 % GGBS blend is significantly higher than for the neat wPC at all measured ages, from ≈4.5 at 7 days, rising to ≈9.0 at 270 days; (v) the values of MCL_{Si} for the C-A-S-H in all the samples are similar and increase slightly with age.

These results agree with previous studies that have shown that, in general, the MCL increases with age and with increases in both Al/Ca and Si/Ca ratios [3,14,24,35,37]. The increase in MCL with age is achieved by the increased occupation of bridging sites in the aluminosilicate chains, and since at any given age the values of MCL_{Si} are similar for the C-A-S-H in the neat wPC pastes and in the blends, the higher value of the MCL observed for the PFA- and slag-containing blends is achieved by additional $Al^{[4]}$ at the bridging sites. It is thus evident that the bridging site is occupied preferentially by $Al^{[4]}$, which is consistent with the conclusion that $Al^{[4]}$ substitutes for $Si^{[4]}$ only in the bridging tetrahedra of the dreierketten chains of C-A-S-H [27,38]. In a study of synthetic C-A-S-H prepared with a high Ca/Si ratio, Kunhi Mohamed et al. [39] associated a peak at 5 ppm on an ^{27}Al spectrum with low intensity at −77 ppm on the ^{29}Si spectrum; they assigned the −77 ppm to paired silicate tetrahedra adjacent to bridging sites occupied by $Al^{[6]}$. If present, such a peak could not be observed in our one-dimensional ^{29}Si NMR because of the severe overlap with the Q^1 peak, and in any case, the absence of significant amounts of $Al^{[6]}$ at bridging sites of the C-A-S-H that is present in hardened cement pastes is indicated by the general agreement between the Al/Si ratios determined by TEM-EDX with those calculated from ^{29}Si NMR when assuming the incorporation of only $Al^{[4]}$

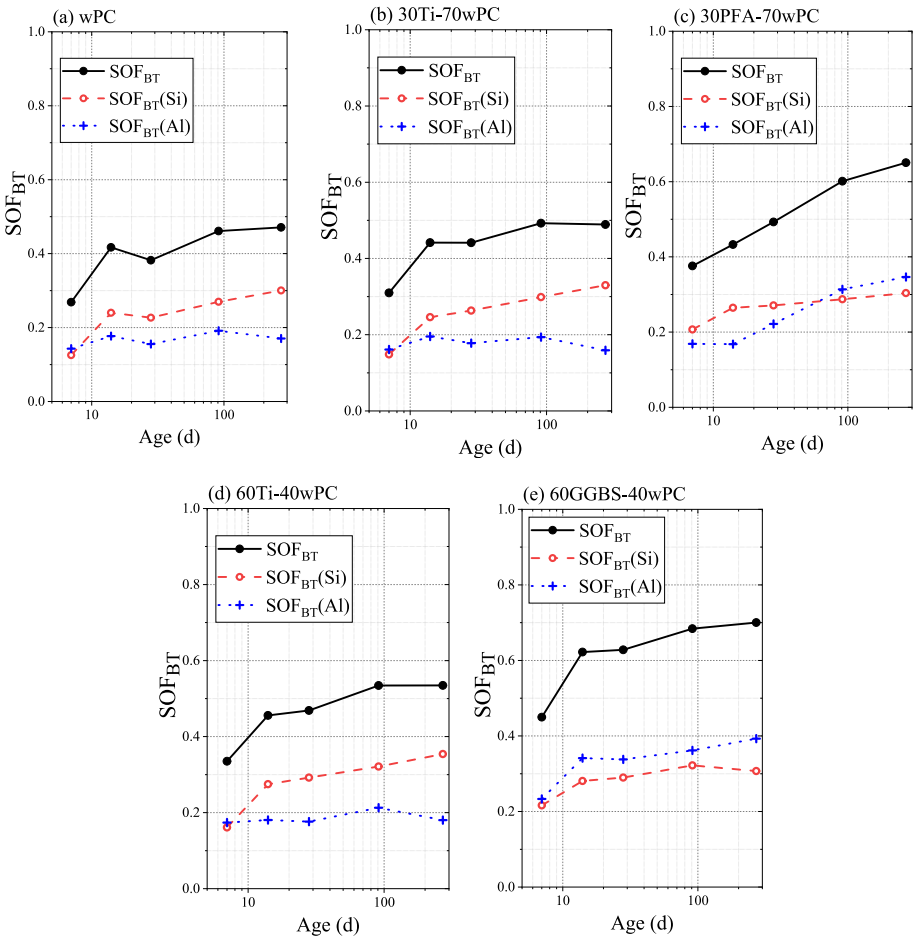

Fig. 10. Site occupancy factor (total) for bridging sites (SOF_{BT}), site occupancy factor for bridging sites by Si^{4+} ($SOF_{BT}(Si)$) or by Al^{3+} ($SOF_{BT}(Al)$). Values are calculated by equations given in [14].

at bridging sites.

The C-S-H that forms in cement systems has linear silicate chains that appear to follow the sequence of dimer, pentamer, octamer … ($3n-1$) (e.g. [35,40]). Since the removal of all, one half and one third of BT from an infinite '*Dreiereinfachketten*' silicate conformation results respectively in linear dimer, pentamer and octamer chains, it is reasonable to assume that lengthening of the chains in C-S-H is achieved by the insertion of BT [2,13,14,28,35,41,42]. Fig. 10 shows how the occupancy factor for the bridging site (SOF_{BT}) [14] varies with age for the C-A-S-H that is present in the samples in this study. The values of SOF_{BT} for all the samples increase with time but the values are significantly higher for the SCMs blends. It is evident that the values for $SOF_{BT}(Si)$ increase gradually as hydration progresses for all the blends, and that this value is comparable with that for the neat wPC and TiO_2 blends. The value of $SOF_{BT}(Si)$ for the SCMs blends is initially slightly higher than for the wPC or TiO_2 blends but at later age (270 days) it is similar (≈0.3). Thus, the lengthening of the aluminosilicate chains (the increase in MCL shown in Fig. 9) is primarily due to an increase in $SOF_{BT}(Al)$ – i.e. the increases in both MCL and Al/Si (Fig. 8) are due to the presence of $Al^{[4]}$ in BT.

Fig. 11 is a plot of the Ca/(Si + Al) against reciprocal MCL for the C-A-S-H present in all the blends examined in this study. The points C-D-E and F-G-H correspond to dimeric jennite- and tobermorite-based structural units that have maximum ($w/n = 2$), intermediate ($w/n = 1$), and minimum ($w/n = 0$) protonation levels. The points U-V-W and X-Y-Z are the same but for infinite chain length [2,41]. Therefore, the quadrilateral area C-E-W-U represents a mixture of jennite-based nanostructure, whereas F-H-Z-X is for tobermorite-based nanostructure [2,41]. Most of the data points fall within the jennite-based area, which suggests that

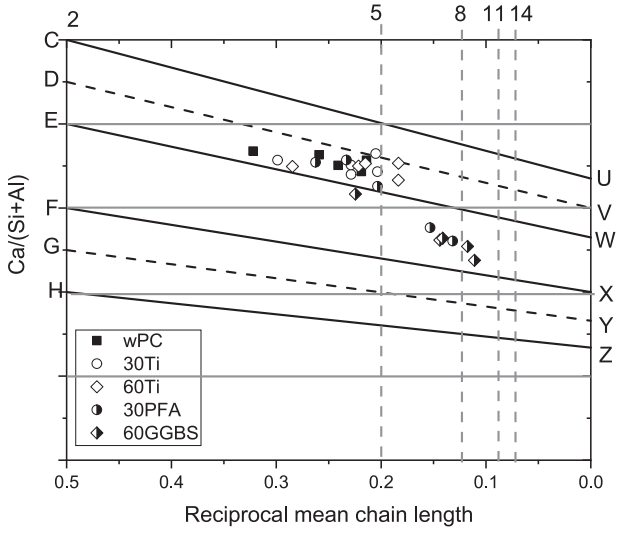

Fig. 11. Relationships between reciprocal mean chain length and the mean Ca/(Si + Al) ratio of the C-A-S-H presented in this study (aged from 7 to 270 days) in blended samples. The Ca/(Si + Al) ratio of C, D, E is 2.50, 2.25, 2.00; for F, G, H is 1.50, 1.25, 1.00; for U, V, W is 1.675, 1.500, 1.325; for X, Y, Z is 1.0, 0.83, 0.67. The details of the explanations and schematic illustrations could be found in [2]. The relationship between the mean chain length and the mean Ca/(Si + Al) ratio of the C-A-S-H is given in Fig. S15.

the nanostructure of the C-A-S-H in those samples can be adequately described using a mixture of jennite-based structural units. However, the points for some SCM blends that have a longer MCL fall between the jennite- and tobermorite-based zones. This finding roughly agrees with the results for various metakaolin-, PFA-, and GGBS-blends that are summarised by Richardson et al. [3], but at earlier ages. In that work, the C-A-S-H with a longer MCL tended to fall into the tobermorite-based nanostructural zone (F-H-Z-X). It is observed that the change in the morphology of C-A-S-H in water-activated SCMs blends starts from the intermediate zone in this figure. The change in morphology is important for durability because of the reduction in the connectivity of the capillary pores and thus reduced permeability. This is discussed in the next section.

Based on the parameters above, Richardson and Groves' model [41] is used here to express the average composition of C-A-S-H gel at different ages based on minimum protonation assumptions. The chemical-structural formulae can be found in the Supplementary materials.

3.4. Morphology and chemical composition of C-A-S-H gel in blended wPC samples

The C-A-S-H that forms in the originally water-filled space (called outer product, OP C-A-S-H) or within the original boundaries of the particles of cement or SCM (called inner product, IP C-A-S-H) have different morphologies. The IP C-A-S-H normally shows fine-scale and homogenous morphology in either alite or blended cement systems [2]. The morphology of OP C-A-S-H in GGBS-, PFA-, and metakaolin-blended cements changes from fibrillar at low Si/Ca and Al/Ca ratios to foil-like at high ratios [3], which is believed to be the reason for permeability improvement in these systems. Indeed, the morphology of OP C-A-S-H directly determines the connectivity of capillary pores that are interlaced by these gel phases. The space constraints, fineness, and aspect ratios of these fibres define the shape, size, and number of capillary pores [3,7,43–45], thus affecting the durability of the structure. Therefore, establishing the reason for the morphological change of OP C-A-S-H is a principal objective in this study.

Fig. 12 shows TEM images that illustrate the typical morphology of OP C-A-S-H in blends containing TiO_2-, PFA, and GGBS at different ages. The ages of the samples selected for the figures (PFA-91, 270d/GGBS-14, 28d) correspond to be the ages where the morphological change of the C-A-S-H occurs due to the reaction of the SCM. The OP C-A-S-H in the TiO_2 blends always had a fibrillar-like morphology illustrated in Fig. 12, which is the typical morphology that is observed throughout the hydration of neat cement or alite [2,7,44,46]. The unchanged morphology indicates that the inert filler does not change the basic nanostructural element of the C-A-S-H gel. The morphology of OP C-A-S-H observed in the PFA and GGBS blends at the ages of 91 and 14 days is similar – i.e. it is thin fibrillar-like. However, after each SCM had reacted to some extent, a change was observed, with the OP C-A-S-H having a much denser/finer fibrillar morphology and some totally foil-like regions. The morphology at this stage is almost always described as 'mixed fine-fibrillar/foil-like morphology' [3]. OP C-A-S-H that has totally foil-like morphology has only been observed in water-activated pastes with 100 % GGBS [2–4,9,19,35], 80 % GGBS-20 % CH [9], or that have relatively large additions of microsilica [47]. In contrast, the OP C-A-S-H is always foil-like in alkali hydroxide-activated pastes, including those of neat Portland cement as well as blends that contain GGBS and PFA [2,3,34]. The micrograph for the PFA blend in Fig. 12 shows an example of a small AFt relict embedded in OP C-A-S-H.

The compositions of the C-A-S-H in the pastes studied in this work are represented on Fig. 11 using mean values, but it is instructive in terms of nanostructural models to also examine the distributions of individual TEM-EDX chemical analyses of OP C-A-S-H on Al/Ca vs. Si/Ca atom ratio plots. For the purpose of direct comparison with the data from this work, Figs. 13 to 15 show the distributions from previous

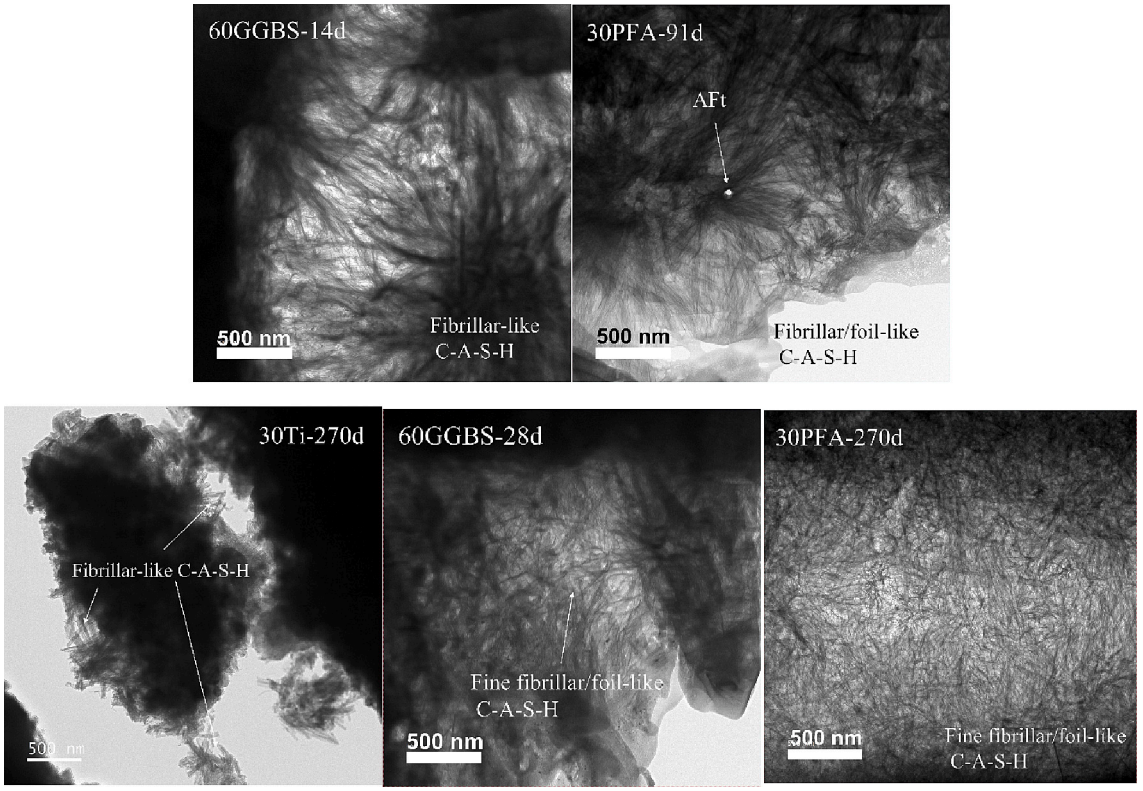

Fig. 12. Bright-field TEM images that show the morphology of C-A-S-H in different samples: 30TiO_2–70wPC at 270 days; 60GGBS-40wPC at 14 and 28 days; 30PFA-70wPC at 91 and 270 days. The TiO_2-containing samples showed unchanged C-A-S-H morphology until 270 days, whilst GGBS/PFA containing samples showed C-A-S-H morphology change between the testing ages.

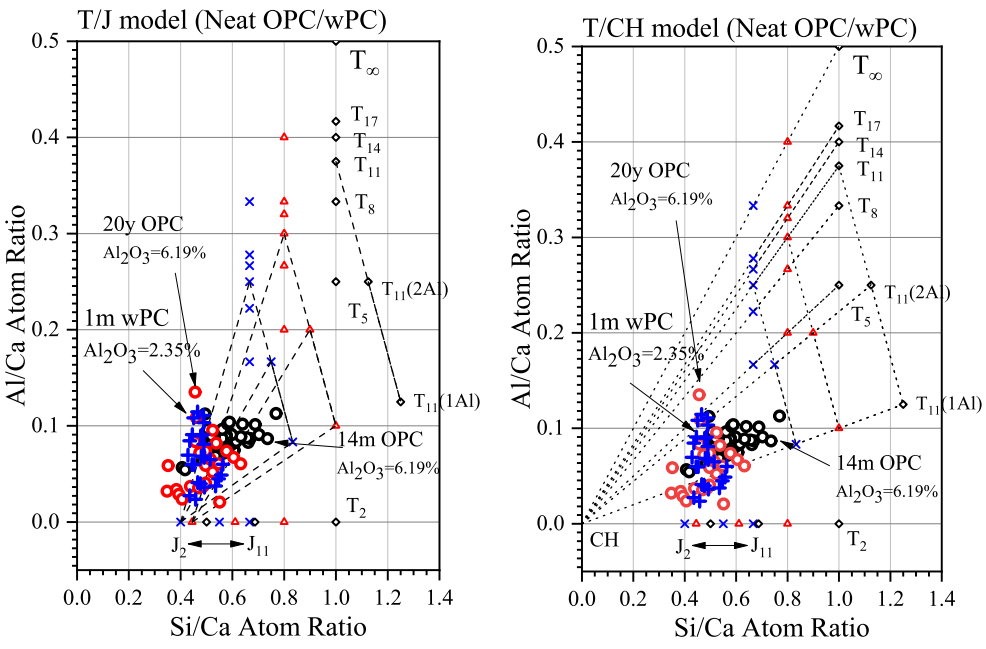

Fig. 13. Summary of TEM-EDX data for OP C-A-S-H in wPC or OPC hydrated for 1 m (month) to 20 y (years). The cross (blue) stands for the wPC hydrated for 1 m at 25 °C; the empty circles stand for OPC hydrated for 14 m and 20 y. Although the Al_2O_3 content for OPC is 6.19 % much higher when compared to that of wPC (2.35 %), the Al/Si ratio did not significantly increase. Additional Al should present in Al-bearing phases such like AFt, AFm, and TAH. Data were taken from [4,48,49]. (For interpretation of the references to color in this figure legend, the reader is referred to the web version of this article.)

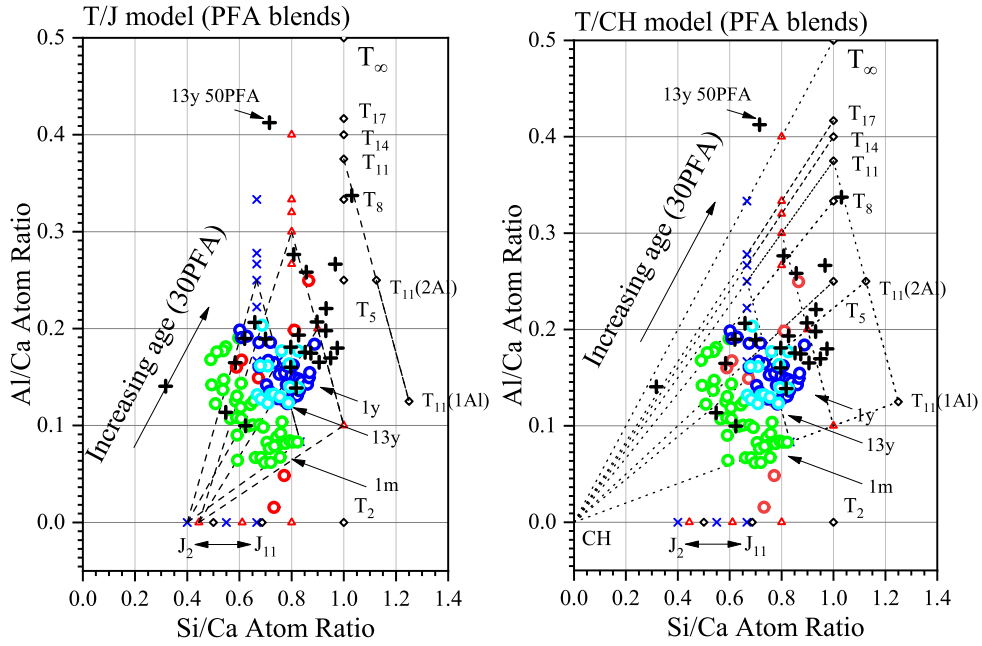

Fig. 14. Summary of TEM-EDX data for OP C-A-S-H in PFA blends hydrated for 28 days to 13 years. The empty circles stand for 30PFA-70wPC blends hydrated for 1 m, 1 year and 13 years; the black cross stands for 50PFA/50wPC hydrated for 13 years.
Data were taken from [3,49,51].

studies of the analyses of OP C-A-S-H in neat OPC pastes, and in blends of OPC with PFA or GGBS [3,4,19,25,34,48,49]. Points are also included that represent the compositions of tobermorite (T-) or jennite-based (J) structural units with the chain lengths of 2, 5, 8, 11, 14, 17, and ∞ [2,28,41]. Three ideal protonation (Si-O-H) levels of the silicate chains are also given: the maximum level (Si/Ca highest; $w/n = 0$), an intermediate level (Si/Ca medium; $w/n = 1$), and the minimum level (Si/Ca lowest; $w/n = 2$). Most of the T_{3n-1} units are saturated with Al at bridging sites (i.e. all bridging tetrahedra in the silicate chain are AlO_4). The exceptions include T_{11}(1Al) or T_{11}(2Al), where only 1 or 2 bridging sites are occupied by Al (i.e. the silicate chain is not saturated with Al; Al/(Al + Si) = 1/11 or 2/11). Since 3 of the 11 tetrahedra in an undecamer single chain are BT, the saturation condition is Al/(Al + Si) = 3/11, which is labelled here simply as T_{11}. The points in the figures for the T_{11} units that have 1, 2 and 3 BT occupied by Al are connected by dash lines.

Data for neat Portland cement pastes and for blends that involve PFA or GGBS are collated separately on Figs. 13, 14 and 15 respectively. All three figures show the Al/Ca-Si/Ca plots from both the T/J and T/CH approaches. The points include pure wPC and OPC hydrated from 1 m (month) to 20 y (years) and the Al_2O_3% content for wPC is 2.4 % and for OPC is 6.2 %. The circles correspond to OPC and the crosses are points for wPC. The scatter points tend towards the points for the J_2 units. The distribution is therefore consistent with the T/J model and may further be associated to fibrillar morphology [2,3]. In addition, the Al/Ca atom

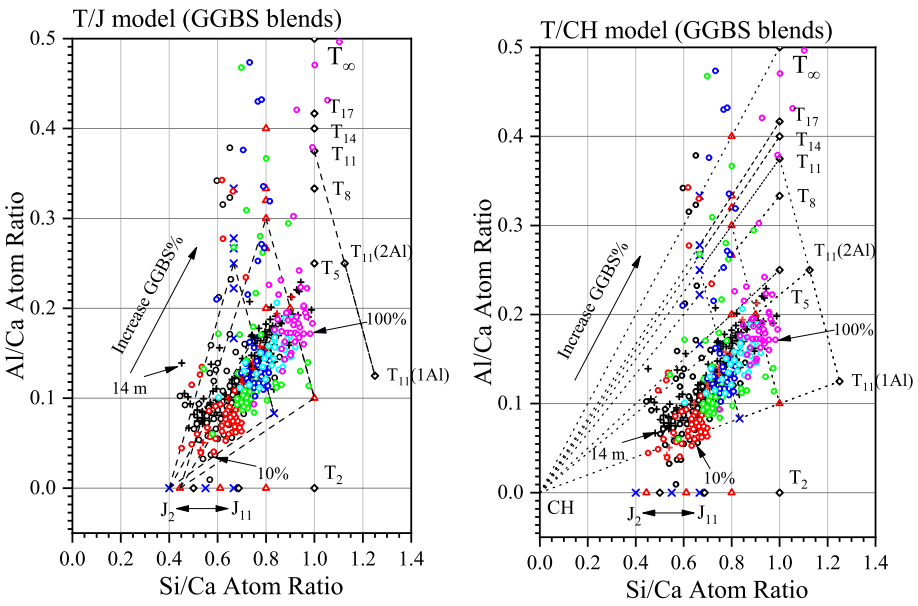

Fig. 15. TEM-EDX data for OP C-A-S-H in GGBS blends hydrated for 14 m to 20 years. The black cross stands for the GGBS/OPC blends hydrated for 14 m; the empty circles stand for the same samples but hydrated for 20 years. The GGBS replacement levels range from 10 % to 100 %. Data were taken from [4,20,34,54].

ratio of C-A-S-H in all pure cement samples is under 0.10 regardless of hydration time or Al content. This can be attributed to there being sufficient Ca in the systems to allow the formation of C-A-S-H with higher Ca/Si ratio. Accordingly, the MCL of these C-A-S-H gels will not increase to a higher level and the incorporation of Al^{3+} is low because of the limited availability of tetrahedral bridging sites in the silicate chains (experimental results show that the MCL for C-S-H gel in high-Ca systems is short, e.g. values of ≈2.75, ≈3.40, and ≈3.60 for C-S-H in β-C_2S, OPC, and C_3S pastes hydrated for ≈1 year with an average Ca/Si ratio ranges from ≈1.7 to 1.9 [9]). Al is instead present in phases such as AFt, AFm, and perhaps TAH [3,50]. The existence of TAH has been questioned recently with the peak on ^{27}Al NMR spectra previously assigned to it attributed instead to $Al^{[6]}$ present at bridging sites in C-A-S-H [36,39]. As noted above, this cannot be a significant mechanism for the incorporation of Al in the C-A-S-H that is present in hardened cement pastes because of the general agreement that has been observed between the Al/Si ratios determined by TEM-EDX with those calculated from ^{29}Si NMR when assuming the incorporation of only $Al^{[4]}$ at bridging sites.

The Al/Ca-Si/Ca data for OP C-A-S-H in PFA-containing pastes are shown in Fig. 14 on plots again representing both the T/J and T/CH points of view. The data are for a 50PFA-50wPC blend (black crosses) hydrated for 13 years, and 30PFA-70wPC blends (unfilled circles) hydrated for 1 m (green), 1 year (dark blue), and 13 years (light blue). A general trend of increasing Al/Ca ratio along with Si/Ca ratio can be observed as hydration time increases. Also, a higher PFA content results in higher Al/Ca and Si/Ca ratios. Comparison of the two plots shows that the TEM-EDX scatter points can be explained by both T/J and T/CH models including data for 30PFA blend hydrated for 1 year and 13 years. In addition, only limited change in Al/Ca ratio is observed for the 30PFA pastes hydrated from 1 year to 13 years, which indicates the hydration degree of PFA is mostly achieved before 1 year. A higher degree of hydration of PFA is reached when cured at a higher temperatures (55 and 85 °C) [25,49,52,53], which results in a slightly higher Al/Ca ratio of OP C-A-S-H.

Fig. 15 shows TEM-EDX data for OP C-A-S-H present in PC-GGBS blends hydrated for 14 m (average values, black cross) and 20 years (scatter points, empty circles) with GGBS loading ranging from 10 % to 100 %. In this case, all data points at lower replacement levels (<10 %) are consistent with the T/J model, whereas those at higher levels can be explained by both the T/J and T/CH models. Increasing the content of GGBS in blends reduces the overall CaO content, and this is reflected in the simultaneous increase in the Al/Ca and Si/Ca ratios of the C-A-S-H. This also happens with hydration time (from 14 m to 20 years) because of continued reaction of the glassy slag (e.g. see Fig. 18 in [4], which shows the reduction in mean Ca/Si ratio).

The distributions on Figs. 13 to 15 of data from previous studies all tend towards to the points for the J_2 units, which means that the TEM-EDX data for C-A-S-H gels that are present in water-activated pastes of neat wPC/OPC, PFA blends, or GGBS blends are all consistent with the T/J nanostructural model. This is different from those in alkali-activated pastes, which show distributions on Al/Ca-Si/Ca plots that tend towards the origin [3], and are thus consistent with a T/CH structural model instead of T/J.

The TEM-EDX data collected during the present study are compared on Fig. 16 with those from previous studies that have already been presented and discussed. Again, many of the new data are consistent with a T/J model with those at higher Al/Ca and Si/Ca values also compatible with a T/CH model [4]. The TiO_2 blends exhibit similar Al/Ca-Si/Ca plots to those for neat wPC. The Al/Ca ratio is always lower than 0.10 and remains stable with age. The structure of C-A-S-H gel in TiO_2 blends can be explained by the combination of T_2/T_5 and J_2/J_5 structural units, which is consistent with the observed short MCL (≈3.0), as shown in Fig. 9. It is evident that for PFA and GGBS blends, most of the points are in agreement with the previous studies.

The Al/Si ratios obtained from NMR and TEM-EDX are compared in Fig. 17 (left). The black-dash diagonal line ($y = x$) is used as a guideline for the relationship. It is clear that all the data are distributed close to the line, indicating a good relationship between the results from TEM-EDX and NMR. This is consistent with results from previous studies involving PFA and GGBS [3], and thus further supports the assumption that is used in the calculation of the Al/Si ratio from ^{29}Si NMR data that there cannot be significant amounts of chain-terminating Al (because that would result in a value from NMR that is greater than that determined by TEM) [27]. Previous studies [3,28,34,55] have shown that there is a universal compositional relationship for the C-A-S-H that is present in cement blends that incorporate aluminosilicate-rich supplementary cementitious materials. This means that in the absence of data from TEM-EDX, it is possible to estimate the Ca/(Si + Al) ratio of C-A-S-H in a PFA- or GGBS-containing cement using that relationship and the value of the Al/Si ratio calculated from the deconvolution of a ^{29}Si NMR

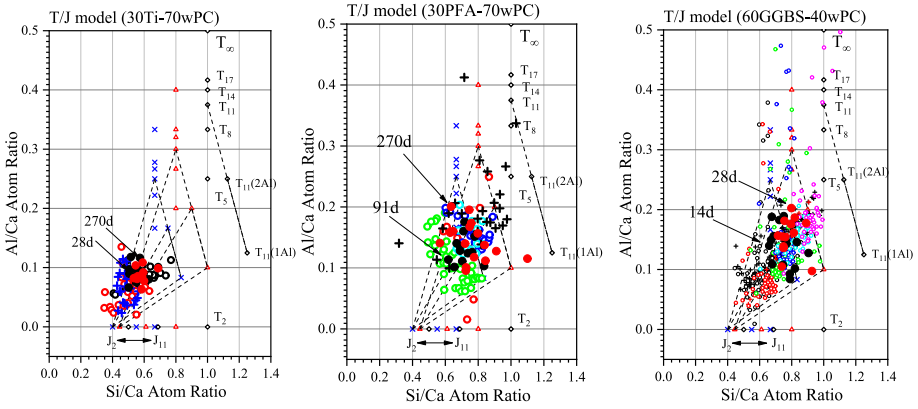

Fig. 16. TEM-EDX data for OP C-A-S-H present in 30TiO_2, 30PFA, and 60GGBS blends hydrated from 14 to 270 days compared with data from previous studies. The black filled circles stand for short-age samples and the red ones stand for long-age samples in individual blend; the symbols for the data from previous studies are explained in the captions for Figs. 13 to 15. (For interpretation of the references to color in this figure legend, the reader is referred to the web version of this article.)

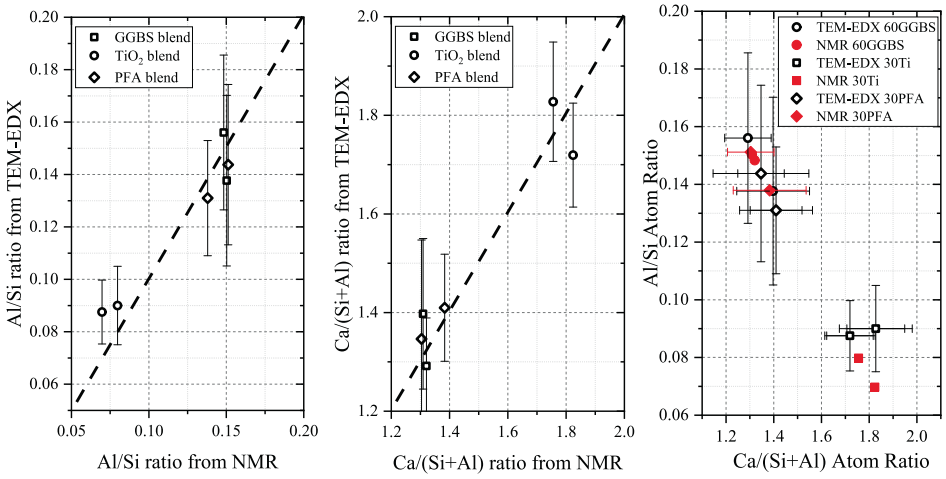

Fig. 17. Relationships of Al/Si ratio (left), Ca/(Si + Al) ratio (middle), and Al/Si-Ca/(Si + Al) (right) calculated from NMR (by using the Al/Si ratio as stated in Fig. 8) and TEM-EDX. The black dash lines stand for y = x function. The error bars stand for the standard deviation from the mean value of each scatter point. It should also be noticed that the ^{29}Si MAS NMR should be collected using quantitative conditions (i.e., sufficient scans and delay time) to ensure the precision of the NMR values.

spectrum. This process is demonstrated for the data from the current study in Fig. 17: the graph in the middle shows the Ca/(Si + Al) ratio from TEM-EDX plotted against the value from NMR, and the right-hand graph is a plot of the Al/Si v Ca/(Si + Al), with points either from TEM-EDX (unfilled symbols) or NMR (solid symbols).

3.5. Pore solution analysis and thermodynamic calculations

Fig. 18 shows the main element concentrations in pore solutions extracted from the blended cement pastes together with the reference lines of chemical compositions from CEM I pore solutions that were compiled by Vollpracht et al. [15]. Since the ICP-OES mainly gives the element concentrations, elements are used in the figures or discussion instead of ions. The Na and K concentrations are crucial for the maintenance of alkalinity of the pore solution but depend mostly on the original chemical compositions of cement. Fig. 18a–b shows that the Na and K concentrations in the current study are lower than the reference CEM I sample. This is attributed to the lower N_2O% and K_2O% contents (0.249 wt% and 0.087 wt%) of the starting wPC when compared to those of CEM I (0.20–0.31 wt% and 0.76–1.03 wt%) [15]. Whilst only limited pore solution data were generated in this study, Fig. 18 shows that the values are in general consistent with the compilation of Vollpracht et al. [15].

The Ca concentration in the pore solution is highly dependent on its counterpart-silicate groups ($H_xSiO_4^{(4-x)}$) and hydroxide ions (OH^-). In most cases, the long-term Ca concentration is below 10 mmol/L, consistent with most previous studies [15,17,23,56–62]; however, in the cement pore solution (wPC) with low pH value, this concentration can reach ≈30 mmol/L and then stabilise at ≈10 mmol/L [56,57]. The data for the pore solution in wPC in this study fall between ≈1 and 10 mmol/L. These values are slightly higher than that of ordinary PC but lower than the wPC in Refs. [56,57]. The reason should still attribute to the alkali content of starting cements, where the high Ca concentration is achieved by 0.13 wt% N_2O and 0.02 wt% K_2O in the starting wPC [56,57]. The general trend of decreasing Ca is identified, which is attributed to the increased alkali concentrations.

The Al concentration is low and hard to detect due to the lower content of C_3A present in wPC (2.1 wt% Al_2O_3) and the high stability of Al/S-bearing phases [63]. Therefore, the Al concentration remains low at ≈0.1 mmol/L and shows a stable trend against time. The addition of GGBS gives a higher concentration of Al.

The Si concentration is crucial for the stability of C-S-H, which is a counterpart to Ca in the pore solutions. The slight increase in the trend can be observed, which is opposite to that of Ca concentration, as expected [64,65]. Moreover, the addition of SCMs will increase the Si concentration.

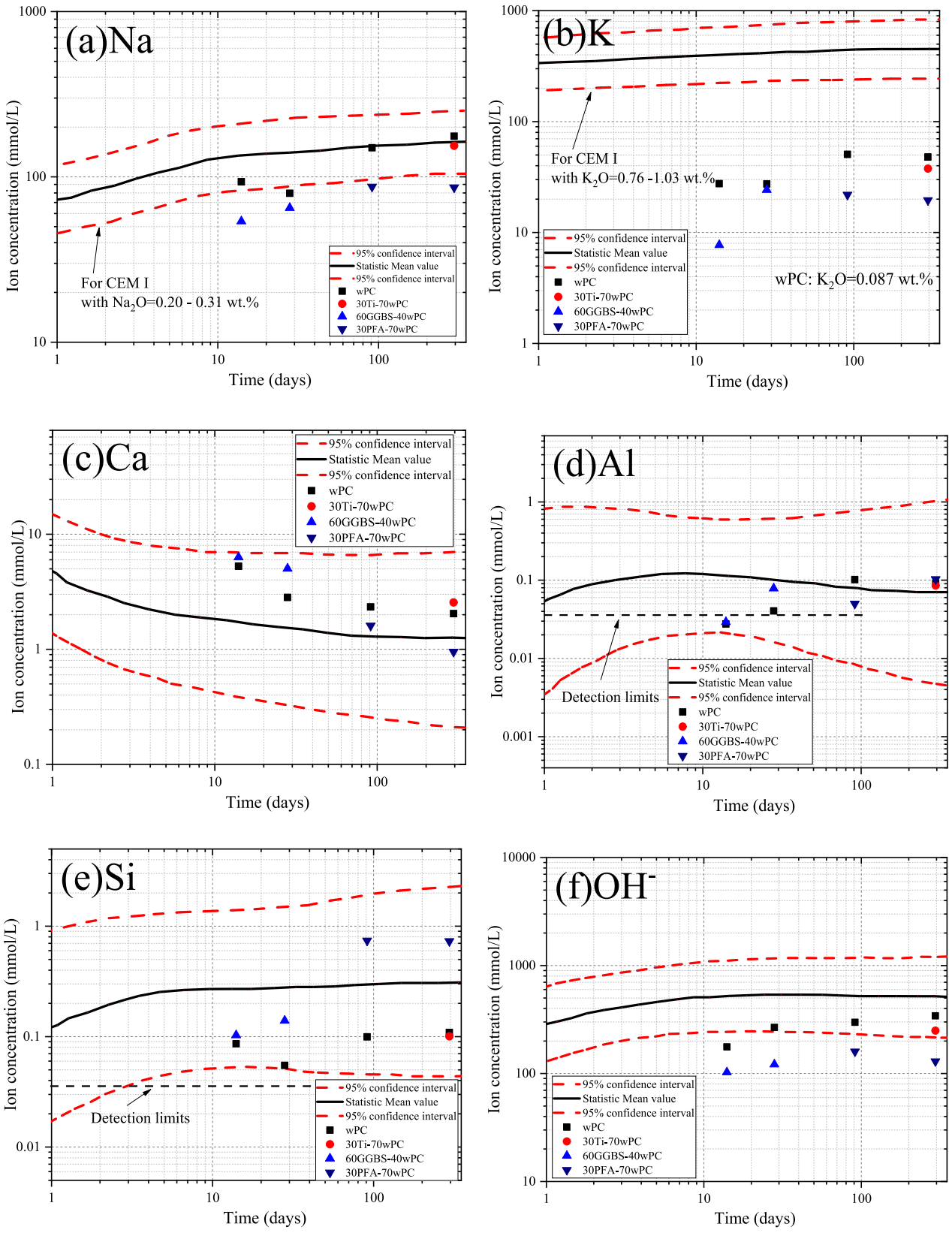

Fig. 18. Chemical compositions of pore solution from blended cement pastes: (a) Na; (b) K; (c) Ca; (d) Al; (e) Si; and (f) hydroxide ion. The concentrations of hydroxide ion refer to the free concentrations based on the measured pH values [58,60,61,66]. The black solid line in each figure stands for the average concentration of individual ion (element) in CEM I system and the red dash lines stand for the 95 % confidence interval as summarised by Vollpracht et al. [15], which is used for comparison with the data generated during the present study. (For interpretation of the references to color in this figure legend, the reader is referred to the web version of this article.)

Finally, the hydroxide ion (OH^-) concentration obtained from the pH values increases as the hydration progresses. This is because the alkali-ions are released from the clinker phases as they react. Therefore, the OH^- should roughly be charge-balanced with that of the sum of free Na and K concentrations. In addition, the increased alkalinity affects the Ca concentration. The relatively lower OH^- concentration when compared to that of CEM I also results from the lower alkali content of the starting cement.

Fig. 19 shows the values of effective saturation index (ESI) for CH in both pure cement systems and blended cements; data from the current study are combined with others compiled from the literature. The general trend of ESI-CH seen in pure cement system starts at ≈0.15 and then stabilises at ≈0.05 at later age. The values drop steeply between 0.2 and 1 day and then gradually decrease until around 10 days. The experimental values from the current study (filled symbols) fall around the stable value after 10 days. In contrast, the SCMs-contained samples have the ESI-CH values that change from positive to negative at long age as hydration progresses as shown in Fig. 19b. The GGBS-containing samples show a higher ESI-CH value than that of pure cement before 1 day, which should be attributed to the initial low pH value of the pore solution that results in a higher Ca concentration. However, as the hydration goes on, this value drops quickly below zero, showing that the continuous consumption of CH happens in such systems. The general tendency gives a linear decrease trend against logarithm of time. It should be noticed that the ESI-CH values at 14 and 28 days are lower than zero, and this coincides with changed morphology (from fibrillar/foil mixture to fine-fibrillar/foil) of C-S-H gels in the system. The black dash-line suggests that the ESI-CH drops down to −0.15 at around 28 days.

Unlike the ESI-CH values in GGBS blends, those in PFA blends stay positive at ages before ~40 days as shown by the red dash line in Fig. 19b. But at later ages, the trend again suggests a value of −0.15 as perhaps the critical value of the morphological change discussed in Section 3.4.

Fig. 20 gives the ESI values of T/J-type C-S-H gels in both pure and blended cement systems. The equilibrium of C-S-H gel depends on the Ca, Si, and OH^- concentrations in the pore solution. For the T-based C-S-H, the higher Ca and OH^- concentrations will result in a lower IAP (ionic activity product) value and thus a lower ESI value. The decreasing trend of ESI-T-C-S-H can be confirmed in pure cement system, which results from the increased pH values of pore solutions. However, for the blended cements, the lower pH values and possible higher Si concentration will maintain a relative higher ESI-T-C-S-H value than that of pure cements. However, no significant trend can be identified from the available values. The experimental data from the current study (solid symbols) support the presence of T-based C-S-H in the blended systems. Fig. 20c–d gives the same information but for J-based C-S-H in both systems. Unlike T-based C-S-H, the higher Ca, Si, and OH- concentrations will result a higher IAP and thus a higher ESI value. Therefore, the decreasing trend of ESI-J-C-S-H must result from the decreasing Ca concentration against time in the pore solution. Similar deceasing trends can be plotted in both pure and blended systems in the range of 0.1 to ≈ 0.4 and 0 to ≈ 0.3 respectively. Some of these values even fall below zero. However, the data in this study gives a relatively higher value, which may be due to the lower pH values obtained by using wPC. One possible link between the morphology-change and the ESI of C-S-H gels may be that the fine-fibrillar/foil-like morphology is associated to the ESI-J-C-S-H < 0.1.

3.6. Discussion on the dominant factors affecting C-A-S-H gel morphology in blended cements

3.6.1. C-A-S-H gel morphology vs. solid phase composition

The Ca/(Si + Al) ratio of C-A-S-H gel remained at ≈1.7–1.9 in the

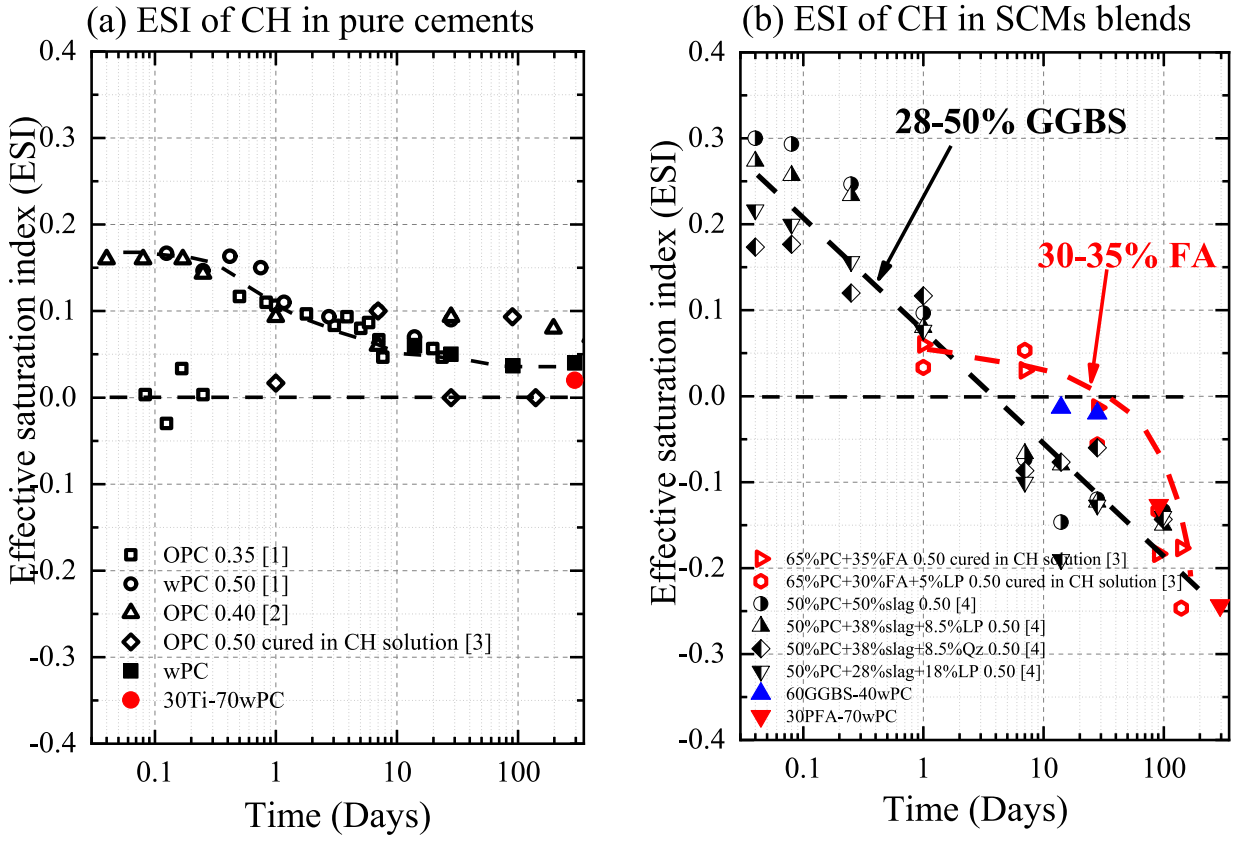

Fig. 19. Effective saturation index (ESI) of CH in different (a) pure cements and (b) blended cements: empty/half-filled symbols are data taken from the literature and solid symbols are data from the current study. The references [1–4] shown in this figure stands for Refs. [11,56,60,67].

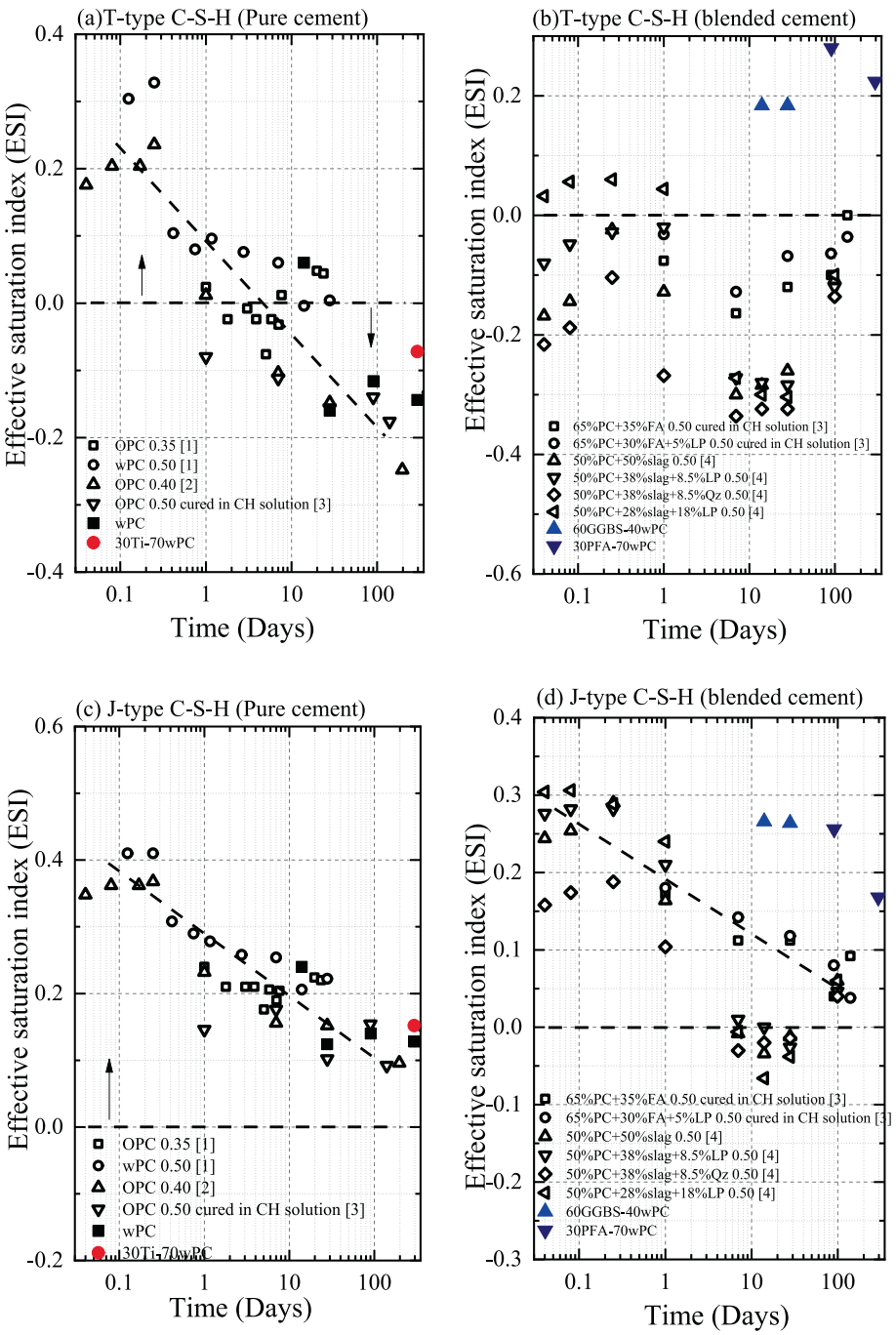

Fig. 20. ESI of different C-S-H gels in pure or blended cements: (a) T-type C-S-H in pure cement; (b) T-type C-S-H in blended cements; (c) J-type C-S-H in pure cement; (d) J-type C-S-H in blended cements. The T-type stands for tobermorite type C-S-H (Ca/Si ratio = 0.83) and the J-type stands for jennite type C-S-H (Ca/Si ratio = 1.67) [17].

pure wPC system (Fig. 8), regardless of the increased CH content (Fig. 2) as the hydration proceeded. The situation is the same in the blends with the TiO_2, whereas in the blends with the SCMs, CH is consumed by the reactions of the glassy slag or fly ash. The presence of fibrillar C-S-H morphology in the TiO_2-blends therefore shows that the absolute CH content in the system is not a direct factor that affects the morphological change of C-A-S-H gel from fibrillar to foil-like. On the other hand, the value of CH^{act}/CH^{exp} can be a reliable factor, which gives information about the amount of CH that is consumed by the SCMs. The critical value for the morphological change appears to be around 0.85 in both the PFA and GGBS blends, which is the same value as reported previously [3].

Fig. 21 shows the changes of Ca/(Si + Al) ratio of C-A-S-H against CH content in the systems studied in this work in combination with the data compiled in [3]. In the SCM blends, the Ca/(Si + Al) ratio decreases as the CH content decreases. The black dash line shows the general trend as a guide for the eye. The data from the current study fall around the line and are centred in the area that is associated with the mixed fibrillar/foil-like morphology. In contrast, the Ca/(Si + Al) ratio does not change with the reduced CH content that occurs with an increase in the amount of inert TiO_2 filler (it remains at ≈1.80), and so those data do not follow the guide line. The C-A-S-H has coarse fibrillar-like morphology regardless of the absolute CH content.

The DoH of the clinker (alite and belite) shows no direct influence on the morphology-change of C-(A-)S-H gel, as shown in Fig. 7. For

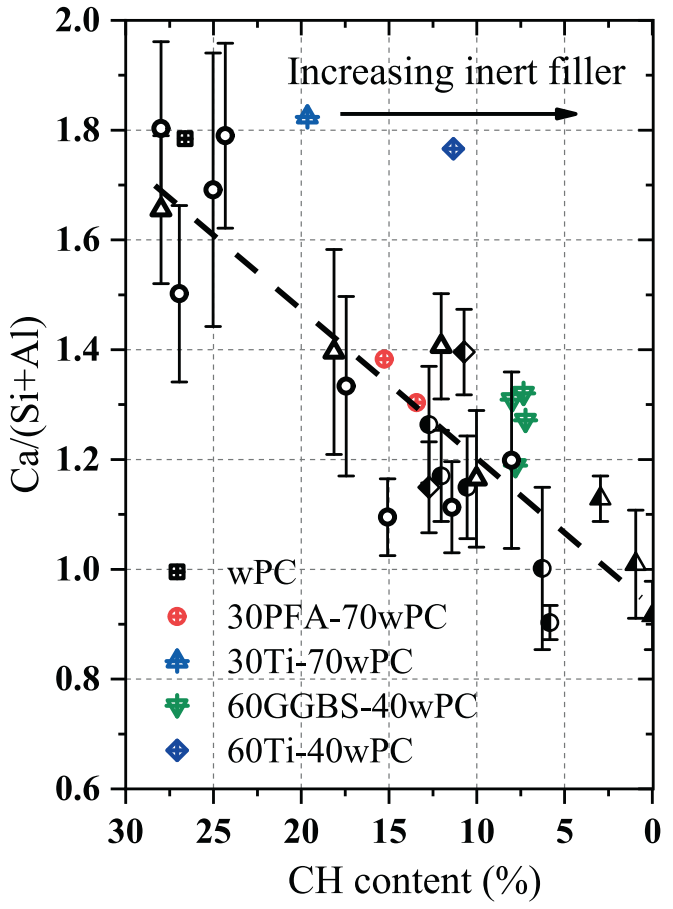

Fig. 21. Relationship between CH content (%) and the Ca/(Si + Al) of C-A-S-H gels that were calculated from the ^{29}Si MAS NMR data as outlined in Section 3.4 and Fig. 17. The data (together with the error bars) were compiled with those from Fig. 24 in [3] together with the guide line. The labels follow those in the literature, i.e. water/KOH-activated PFA (circles), metakaolin (diamond), or GGBS (triangle) (open symbol = entirely fibrillar morphology; half-filled symbol = mixed fibrillar/foil-like morphology; filled symbol = entirely foil-like). Data from the current study are labelled with the symbols with a cross inside. Only data from mature blends are used for comparison, i.e. wPC and TiO_2 blends hydrated for 270 days; PFA blends hydrated for 91 days and 270 days; GGBS blends hydrated for >14 days.

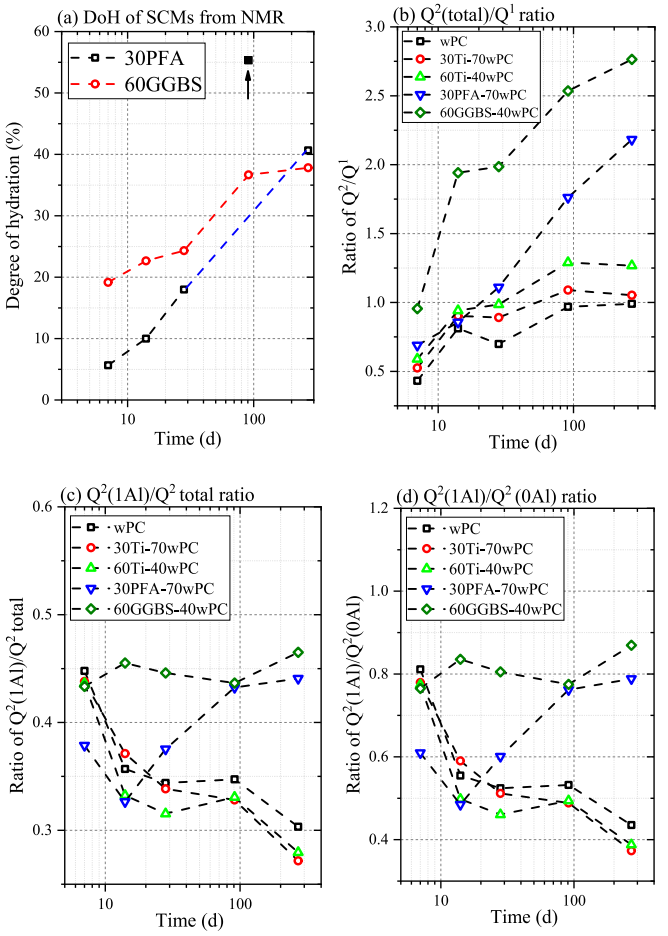

Fig. 22. Further information calculated from ^{29}Si MAS NMR: (a) hydration degree of SCMs (ignoring the sidebands, which will result a lower value than expected, see Fig. S14 (Supplementary materials)). The filled square (30PFA-91d) was not connected in the curve because it was affected by the sideband-effect of PFA, which resulted in experimental error during the deconvolution; (b) Q^2(total)/Q^1 ratio; (c) Q^2(1Al)/Q^2(total) ratio (proportion of Q^2(1Al) units in all Q^2 units); and (d) Q^2(1Al)/Q^2(0Al).

example, the DoH of clinker in TiO_2-containing samples were much higher than those in samples containing SCMs at later ages; however, the morphology of C-A-S-H remained fibrillar. Whilst the morphology-change is affected by the DoH of the SCMs, it depends on the replacement ratio, reactivity, and chemical compositions of the SCM used. Fig. 22a gives the DoH of PFA and GGBS in the blends from NMR (but ignoring the sidebands); both increase with time and thus contribute to the change in the composition of the C-A-S-H.

3.6.2. *C-A-S-H morphology vs. its nanostructure*

As shown by the experimental observations given in Sections 3.3–3.4, the nanostructure of C-A-S-H has crucial effects on its morphology. The foil-like morphology is linked with the long MCL of ≈ 7–8 and with increased incorporation of Al (average Ca/(Si + Al) ratio < 1.30 and Al/Si > 0.15), which are both associated with increased T-based structure. A value of Q^2(1Al) > 30 % appears to be associated with the change in morphology. Fig. 22b–d shows some further comparison of Q^2(1Al) and other Q^2 units, which give more parameters related to the above value. Specifically, Q^2(total)/Q^1 ratio > 2.0, Q^2(1Al)/Q^2(total) > 0.45, and Q^2(1Al)/Q^2(0Al) > 0.80 are three related parameters that affect the morphological change. In addition, the SOF factors can also be used as the indicator for morphological change when SOF_{BT} > 0.60 or SOF_{BT}(Al) > 0.30.

4. Summary

The factors that affect the morphological change of C-A-S-H gel that occurs in blended cements were investigated. Two SCMs (PFA, GGBS) and one inert filler (TiO_2) were blended with wPC. It was found that the morphology of C-A-S-H in cements containing the SCMs changed from fibrillar-like to mixed fine-fibrillar/foil-like, whilst in pure or inert-filler blended cements it remained fibrillar throughout hydration. The solid and liquid phases were characterised using multiple techniques to better understand the reasons for the change in morphology. The main observations are summarised as follows:

(a) The C-A-S-H morphology-change happens in 60%GGBS blends within 14–28 days and in 30%PFA blends within 91–270 days.
(b) The C-A-S-H morphology-change is dominated by its chemical composition, nanostructure, and solution environment.
(c) The morphology-change happens when CH^{act}/CH^{exp} < 0.85.
(d) The foil-like morphology appears when the C-A-S-H gels show the following characteristics: Ca/(Si + Al) ratio < 1.3 and Al/Si ratio > 0.15; the MCL ≈ 7–8; the SOF_{BT} > 0.6 or SOF_{BT}(Al) > 0.3; the

proportion of $Q^2(1Al) > 30$ %; $Q^2(total)/Q^1$ ratio > 2.0; $Q^2(1Al)/Q^2(total)$ ratio > 0.45; $Q^2(1Al)/Q^2(0Al)$ ratio > 0.80.

(e) The foil-like morphology appears when the pore solutions show the following characteristics: ESI of CH < -0.15 and ESI of J-based C-A-S-H gel < 0.1.

(f) The DoH of clinker (alite + belite) and the absolute CH content are not direct factors related to foil-like morphology. The DoH of SCMs depends on their replacement ratio, activity, and chemical compositions.

CRediT authorship contribution statement

Xiaohong Zhu: Conceptualization, Methodology, Investigation, Data curation, Formal analysis, Writing – original draft, Writing – review & editing. **Ian G. Richardson:** Conceptualization, Methodology, Supervision, Project administration, Funding acquisition, Resources, Validation, Writing – review & editing.

Declaration of competing interest

The authors declare that they have no known competing financial interests or personal relationships that could have appeared to influence the work reported in this paper.

Data availability

Data will be made available on request.

Acknowledgements

The first author gratefully acknowledges the financial support of the CSC-Leeds Joint Scholarship (Grant No. CSC2017050152). The facilities provided by UKCRIC National Centre for Infrastructure Materials at the University of Leeds are highly appreciated. The first author also would like to thank Ms. Victoria Leadley for the help on the NMR experiments and Ms. Lucy Leonard and Mr. Leslie Arkless for the trainings on XRD, STA, and glovebox. The suggestions during the experimental design and the revisions of this manuscript from Prof. Phil Purnell (University of Leeds) are highly acknowledged.

Appendix A. Supplementary data

Supplementary data to this article can be found online at https://doi.org/10.1016/j.cemconres.2023.107156.

References

[1] M.C.G. Juenger, R. Snellings, S.A. Bernal, Supplementary cementitious materials: new sources, characterization, and performance insights, Cem. Concr. Res. 122 (2019) 257–273.
[2] I.G. Richardson, Tobermorite/jennite- and tobermorite/calcium hydroxide-based models for the structure of C-S-H: applicability to hardened pastes of tricalcium silicate, β-dicalcium silicate, Portland cement, and blends of Portland cement with blast-furnace slag, metakaolin, or silica fume, Cem. Concr. Res. 34 (9) (2004) 1733–1777.
[3] I.G. Richardson, et al., Hydration of water- and alkali-activated white Portland cement pastes and blends with low-calcium pulverized fuel ash, Cem. Concr. Res. 83 (2016) 1–18.
[4] R. Taylor, I.G. Richardson, R.M.D. Brydson, Composition and microstructure of 20-year-old ordinary Portland cement–ground granulated blast-furnace slag blends containing 0 to 100% slag, Cem. Concr. Res. 40 (7) (2010) 971–983.
[5] J. Li, et al., Influences of cross-linking and Al incorporation on the intrinsic mechanical properties of tobermorite, Cem. Concr. Res. 136 (2020), 106170.
[6] J. Li, W. Zhang, P.J.M. Monteiro, Synchrotron X-ray raman scattering shows the changes of the ca environment in C-S-H exposed to high pressure, Cem. Concr. Res. 132 (2020), 106066.
[7] Z. Zhang, G.W. Scherer, A. Bauer, Morphology of cementitious material during early hydration, Cem. Concr. Res. 107 (2018) 85–100.
[8] J. Li, et al., Fibrillar calcium silicate hydrate seeds from hydrated tricalcium silicate lower cement demand, Cem. Concr. Res. 137 (2020), 106195.
[9] I.G. Richardson, The nature of the hydration products in hardened cements, Cem. Concr. Compos. 22 (2000) 97–113.
[10] E. Tajuelo Rodriguez, et al., Composition, silicate anion structure and morphology of calcium silicate hydrates (C-S-H) synthesised by silica-lime reaction and by controlled hydration of tricalcium silicate (C3S), Adv. Appl. Ceram. 114 (7) (2015) 362–371.
[11] S. Adu-Amankwah, et al., Influence of limestone on the hydration of ternary slag cements, Cem. Concr. Res. 100 (2017) 96–109.
[12] K. Scrivener, R. Snellings, B. Lothenbach, in: K. Scrivener, R. Snellings, B. Lothenbach (Eds.), A Practical Guide to Microstructural Analysis of Cementitious Materials, CRC Press, Boca Raton, 2016.
[13] A.R. Brough, et al., In situ solid-state NMR studies of Ca3SiO5: hydration at room temperature and at elevated temperatures using 29Si enrichment, J. Mater. Sci. 29 (1994) 3926–3940.
[14] I.G. Richardson, Model structures for C-(A)-S-H(I), Acta Crystallogr. Sect. B: Struct. Sci. Cryst. Eng. Mater. 70 (Pt 6) (2014) 903–923.
[15] A. Vollpracht, et al., The pore solution of blended cements: a review, Mater. Struct. 49 (8) (2015) 3341–3367.
[16] J.R. Dean, in: D.J. Ando (Ed.), Practical Inductively Coupled Plasma Spectrocopy Analytical Techniques in the Sciences (AnTS), John Wiley & Sons Ltd, England, 2005.
[17] B. Lothenbach, Thermodynamic equilibrium calculations in cementitious systems, Mater. Struct. 43 (10) (2010) 1413–1433.
[18] I.G. Richardson, C.R. Wilding, M.J. Dickson, The hydration of blastfurnace slag cements, Adv. Cem. Res. 2 (8) (1989) 147–157.
[19] I.G. Richardson, G.W. Groves, Microstructure and microanalysis of hardened cement pastes involving ground granulated blast-furnace slag, J. Mater. Sci. 27 (1992) 6204–6212.
[20] I.G. Richardson, J.G. Cabrera, The nature of C-S-H in model slag-cements, Cem. Concr. Compos. 22 (2000) 259–266.
[21] E. Berodier, K. Scrivener, G. Scherer, Understanding the filler effect on the nucleation and growth of C-S-H, J. Am. Ceram. Soc. 97 (12) (2014) 3764–3773.
[22] J. Skibsted, R. Snellings, Reactivity of supplementary cementitious materials (SCMs) in cement blends, Cem. Concr. Res. 124 (2019).
[23] B. Lothenbach, K. Scrivener, R.D. Hooton, Supplementary cementitious materials, Cem. Concr. Res. 41 (12) (2011) 1244–1256.
[24] I.G. Richardson, The calcium silicate hydrates, Cem. Concr. Res. 38 (2) (2008) 137–158.
[25] A.V. Girão, et al., Composition, morphology and nanostructure of C-S–H in 70% white Portland cement–30% fly ash blends hydrated at 55°C, Cem. Concr. Res. 40 (9) (2010) 1350–1359.
[26] I.G. Richardson, S. Li, Composition and structure of an 18-year-old 5M KOH-activated ground granulated blast-furnace slag paste, Constr. Build. Mater. 168 (2018) 404–411.
[27] I.G. Richardson, et al., Location of aluminum in substituted calcium silicate hydrate (C-S-H) gels as determined by 29Si and 27Al NMR and EELS, J. Am. Ceram. Soc. 76 (9) (1993) 2285–2288.
[28] I.G. Richardson, G.W. Groves, The incorporation of minor and trace elements into calcium silicate hydrate gel in hardened cement pastes, Cem. Concr. Res. 23 (1993) 131–138.
[29] E. Lippmma, et al., Structural studies of silicates by solid-state high-resolution silicon-29 NMR, J. Am. Ceram. Soc. 102 (1980) 4889–4893.
[30] E. Lippmma, et al., A high resolution 29Si NMR study of the hydration of tricalciumsilicate, Cem. Concr. Res. 12 (1982) 597–602.
[31] X. Cong, R.J. Kirkpatrick, 17O and 29Si MAS NMR study of β-C2S hydration and the structure of calcium-silicate-hydrates, Cem. Concr. Res. 23 (1993) 1065–1077.
[32] X. Cong, R.J. Kirkpatrick, 29Si MAS NMR study of the structure of calcium silicate hydrate, Adv. Cem. Based Mater. 3 (1996) 144–156.
[33] M.D. Andersen, H.J. Jakobsen, J. Skibsted, Incorporation of aluminum in the calcium silicate hydrate (C−S−H) of hydrated Portland Cements_ a high-field 27Al and 29Si MAS NMR investigation, Inorg. Chem. 42 (2003) 2280–2287.
[34] I.G. Richardson, G.W. Groves, The structure of the calcium silicate hydrate phases present in hardened pastes of white Portland cement GGBFS, J. Mater. Sci. 32 (1997) 4793–4802.
[35] I.G. Richardson, The nature of C-S-H in hardened cements, Cem. Concr. Res. 29 (1999) 1131–1147.
[36] S.-Y. Yang, et al., Incorporation of sodium and aluminum in cementitious calcium-alumino-silicate-hydrate C-(A)-S-H phases studied by 23Na, 27Al, and 29Si MAS NMR spectroscopy, J. Phys. Chem. C 125 (51) (2021) 27975–27995.
[37] J.J. Chen, The Nanostructure of Calcium Silicate Hydrate, in Feild of Materials Science and Engineering, Northwestern University USA, 2003.
[38] M.D. Andersen, H.J. Jakobsen, J. Skibsted, Characterization of white Portland cement hydration and the C-S-H structure in the presence of sodium aluminate by 27Al and 29Si MAS NMR spectroscopy, Cem. Concr. Res. 34 (5) (2004) 857–868.
[39] A. Kunhi Mohamed, et al., The atomic-level structure of cementitious calcium aluminate silicate hydrate, J. Am. Chem. Soc. 142 (25) (2020) 11060–11071.
[40] J. Hirljac, Z.-Q. Wu, J. Young, Silicate polymerization during the hydration of alite, Cem. Concr. Res. 13 (6) (1983) 877–886.
[41] I.G. Richardson, G.W. Groves, Models for the composition and structure of calcium silicate hydrate (C-S-H) gel in hardened tricalcium silicate pastes, Cem. Concr. Res. 22 (1992) 1101–1110.
[42] E. Tajuelo Rodriguez, et al., Thermal stability of C-S-H phases and applicability of Richardson and Groves' and Richardson C-(A)-S-H(I) models to synthetic C-S-H, Cem. Concr. Res. 93 (2017) 45–56.
[43] T.D. Ciath, E.G. Swenson, Morphology and microstructure of hydrating Portland cement and its constituents I. Changes in hydration of tricalcium aluminate alone and in the presence of triethanolamine or calcium lignosulphonate, Cem. Concr. Res. 1 (1971) 143–158.

[44] M. Collepardi, B. Marchese, Morphology and surface properties of hydrated tricalcium silicate pastes, Cem. Concr. Res. 2 (1972) 57–65.
[45] P.C. Fonseca, H.M. Jennings, The effect of drying on early-age morphology of C-S–H as observed in environmental SEM, Cem. Concr. Res. 40 (12) (2010) 1673–1680.
[46] E.T. Rodriguez, Relation between Composition, Structure and Morphology in C-S-H, in School of Civil Engineering, University of Leeds, UK, 2015.
[47] G.W. Groves, S.A. Rodger, The hydration of C3S and ordinary Portland cement with relatively large additions of microsilica, Adv. Cem. Res. 2 (8) (1989) 135–140.
[48] I.G. Richardson, G.W. Groves, Microstructure and microanalysis of hardened ordinary Portland cement pastes, J. Mater. Sci. 28 (1993) 265–277.
[49] A.V. Girao, The Nanostrructure and Degradation of Csh in Portland and Blended Cements, in School of Civil Engineering, University of Leeds, UK, 2007.
[50] S. Jia, I.G. Richardson, Micro- and nano-structural evolutions in white Portland cement/pulverized fuel ash cement pastes due to deionized-water leaching, Cem. Concr. Res. 103 (2017) 191–203.
[51] S. Jia, Micro/Nano-Structural Evolution in Blended Cement Paste Due to Prograssive Deionised Water Leaching, in School of Civil Engineering, University of Leeds, UK, 2014.
[52] A.V. Girao, et al., Morphology and nanostructure C-S–H in white Portland cement–fly ash hydrated at 85°C, Adv. Appl. Ceram. 106 (6) (2007) 283–293.
[53] A.V. Girão, et al., Composition, morphology and nanostructure of C-S–H in white Portland cement pastes hydrated at 55 °C, Cem. Concr. Res. 37 (12) (2007) 1571–1582.
[54] R. Taylor, I.G. Richardson, R.M.D. Brydson, Nature of C-S–H in 20 year old neat ordinary Portland cement and 10% Portland cement–90% ground granulated blast furnace slag pastes, Adv. Appl. Ceram. 106 (6) (2013) 294–301.
[55] I.G. Richardson, et al., The characterization of hardened alkali activated slag paste and the nature of the calcium silicate hydrate phase, Cem. Concr. Res. 24 (5) (1994) 813–829.
[56] D. Rothstein, et al., Solubility behavior of ca-, S-, Al-, and si-bearing solid phases in Portland cement pore solutions as a function of hydration time, Cem. Concr. Res. 32 (2002) 1663–1671.
[57] J.J. Thomas, et al., Effect of hydration temperature on the solubility behavior of ca-, S-, Al-, and si-bearing solid phases in Portland cement pastes, Cem. Concr. Res. 33 (12) (2003) 2037–2047.
[58] B. Lothenbach, F. Winnefeld, Thermodynamic modelling of the hydration of Portland cement, Cem. Concr. Res. 36 (2) (2006) 209–226.
[59] B. Lothenbach, et al., Effect of temperature on the pore solution, microstructure and hydration products of Portland cement pastes, Cem. Concr. Res. 37 (4) (2007) 483–491.
[60] B. Lothenbach, et al., Influence of limestone on the hydration of Portland cements, Cem. Concr. Res. 38 (6) (2008) 848–860.
[61] B. Lothenbach, et al., Thermodynamic modelling of the effect of temperature on the hydration and porosity of Portland cement, Cem. Concr. Res. 38 (1) (2008) 1–18.
[62] D. Damidot, et al., Thermodynamics and cement science, Cem. Concr. Res. 41 (7) (2011) 679–695.
[63] R.J. Myers, et al., Solution chemistry of cubic and orthorhombic tricalcium aluminate hydration, Cem. Concr. Res. 100 (2017) 176–185.
[64] B. Lothenbach, A. Nonat, Calcium silicate hydrates: solid and liquid phase composition, Cem. Concr. Res. 78 (2015) 57–70.
[65] H.M. Jennings, Aqueous solubility relationships for two types of calcium silicate hydrate, J. Am. Ceram. Soc. 69 (8) (1986) 614–618.
[66] B. Lothenbach, E. Wieland, A thermodynamic approach to the hydration of sulphate-resisting Portland cement, Waste Manag. 26 (7) (2006) 706–719.
[67] K. De Weerdt, et al., Hydration mechanisms of ternary Portland cements containing limestone powder and fly ash, Cem. Concr. Res. 41 (3) (2011) 279–291.